





# Lunar Low-Titanium Magmatism During Ancient Expansion Inferred From Ejecta Originating From Linear Gravity Anomalies

G. Nishiyama<sup>1,2,3</sup> , T. Morota<sup>3</sup> , N. Namiki<sup>2,3,4</sup> , K. Inoue<sup>3</sup>, and S. Sugita<sup>3</sup> 

<sup>1</sup>Institute of Planetary Research, German Aerospace Center (DLR), Berlin, Germany, <sup>2</sup>National Astronomical Observatory of Japan, Mitaka, Japan, <sup>3</sup>Department of Earth and Planetary Science, The University of Tokyo, Tokyo, Japan, <sup>4</sup>The Graduate University for Advanced Studies, SOKENDAI, Hayama, Japan

### Key Points:

- High-calcium pyroxene exposures and gravity reduction around Roche crater imply an excavation of lunar linear gravity anomaly materials
- Lunar subsurface dikes formed during the ancient expansion stage are estimated to be composed of low-titanium magma
- A linear gravity anomaly possibly postdates the Rowland crater, suggesting a potential prolongation of lunar expansion beyond the Nectarian age

### Supporting Information:

Supporting Information may be found in the online version of this article.

### Correspondence to:

G. Nishiyama,  
[gaku.nishiyama@dlr.de](mailto:gaku.nishiyama@dlr.de)

### Citation:

Nishiyama, G., Morota, T., Namiki, N., Inoue, K., & Sugita, S. (2024). Lunar low-titanium magmatism during ancient expansion inferred from ejecta originating from linear gravity anomalies. *Journal of Geophysical Research: Planets*, 129, e2023JE008034. <https://doi.org/10.1029/2023JE008034>

Received 29 JUL 2023

Accepted 11 SEP 2024

### Author Contributions:

**Conceptualization:** G. Nishiyama,

T. Morota, N. Namiki

**Formal analysis:** G. Nishiyama

**Funding acquisition:** G. Nishiyama,

S. Sugita

**Investigation:** G. Nishiyama, K. Inoue

**Methodology:** G. Nishiyama, T. Morota

**Supervision:** T. Morota, N. Namiki,

S. Sugita

**Validation:** K. Inoue

**Visualization:** G. Nishiyama

**Writing – original draft:** G. Nishiyama

**Writing – review & editing:** T. Morota,

N. Namiki, S. Sugita

**Abstract** Linear gravity anomalies (LGAs) on the Moon have been interpreted as ancient magmatic intrusions formed during the lunar expansion. The composition of such ancient subsurface intrusions may offer hints for the lunar thermodynamic state in the initial stage of lunar history. To pose a first compositional constraint on magmatism related to lunar expansion, this study analyzed the spectrum and gravity around craters on LGAs, such as Rowland, Roche, and Edison craters. Using reflectance spectra around the craters, we first surveyed non-mare basaltic exposures. To test the LGA excavation scenario as a possible origin of the discovered exposures, we then compared the Gravity Recovery and Interior Laboratory data and post-cratering gravity simulation with the iSALE shock physics code. Our spectral analysis reveals no basaltic exposure around the Rowland crater. Further, the observed termination of LGA at the crater rim contradicts the gravity simulation, which assumes that LGA predates the Rowland crater. These results suggest that LGA formation might postdate the Rowland formation and that lunar expansion lasted even after the Nectarian age. On the other hand, we found that both Roche and Edison craters possess basaltic exposures in their peripheries. Because the gravity reduction inside Roche crater can be reproduced in our simulation, the discovered basaltic exposures are possibly LGA materials ejected from these craters. The composition of those exposures shows that the LGA intrusions at the two locations are composed of low-titanium magma, indicating that ancient magma during the expansion did not contain ilmenite-rich melt, perhaps resulting from the low-ilmenite content of the ancient upper mantle.

**Plain Language Summary** The Moon has positive, narrow, and long gravity anomalies, so-called linear gravity anomalies (LGAs), which are thought to be magmatic intrusions formed during the ancient lunar expansion. The composition of these intrusions may provide insights into the early lunar thermal state. This study analyzed the reflectance spectra and gravity data around craters located on LGAs, specifically Rowland, Roche, and Edison craters, which are postulated to have ejected the LGA material. By analyzing the reflectance spectra, we first identified non-mare basaltic exposures that likely originated from these subsurface formations. We next examine if these exposures are composed of the LGA materials by comparing the observed gravity with cratering simulation results. We found no basaltic exposures around Rowland and that gravity inside Rowland is not consistent with the excavation hypothesis, perhaps suggesting that LGA formation and lunar expansion occurred after the Rowland formation. On the other hand, we discovered basaltic exposures around both Roche and Edison craters, which can be interpreted as ejecta from the LGAs consistent with the gravity inside Roche crater. The composition of these exposures indicates that LGAs are composed of low-titanium magma, which provides a new constraint on the ancient thermal state of the Moon.

## 1. Introduction

The early expansion stage of the Moon following its formation is crucial to comprehend the thermal evolution of the lunar interior. A number of lunar evolutionary models have proposed that the Moon might have undergone an expansion phase in its thermal history (Laneuville et al., 2013; U et al., 2022; N. Zhang et al., 2013a, 2013b). Petrological studies have indicated that the Moon had a layer of ilmenite-bearing cumulates (IBC) between its anorthositic crust and olivine-orthopyroxene mantle immediately following the solidification of the lunar magma ocean (Elkins-Tanton et al., 2011; Snyder et al., 1992). It has been hypothesized that this dense layer drove gravitational instability, which subsequently results in a mantle overturn and the release of gravitational potential

© 2024. The Author(s).

This is an open access article under the terms of the [Creative Commons Attribution License](https://creativecommons.org/licenses/by/4.0/), which permits use, distribution and reproduction in any medium, provided the original work is properly cited.

Attribution License, which permits use, distribution and reproduction in any medium, provided the original work is properly cited.

into heat. This overturn process has been believed to account for multiple lunar geologic features, such as the Mg-suite magmatism (e.g., Prissel et al., 2023; Shearer et al., 2015). The overturn may have simultaneously transported heat-producing elements to the lunar core-mantle boundary zone, producing radiogenic heat in the deep area of the Moon (e.g., Hess & Parmentier, 1995). The following rise in the lunar temperature may have caused thermal expansion of the total volume in the early stage of the Moon (Laneuville et al., 2013; N. Zhang et al., 2013a, 2013b). This process coincides with the melt generation and migration, which may also contribute to the lunar volumetric change (U et al., 2022). The duration of lunar radius change depends on the initial thermal state and inner structure of the Moon. Therefore, temporal constraints on ancient lunar expansion are essential to elucidate thermal history.

The composition of the produced magma during the lunar expansion is also significant for understanding the source properties and related evolutionary processes inside the Moon. Maria on the lunar surface consists of volcanic basalt, whose ages have a peak at 3.2–3.8 Ga and another peak around 2.0 Ga in the Procellarum KREEP Terrain (PKT) region (e.g., Hiesinger et al., 2003; Morota et al., 2011). The composition of lunar maria, particularly titanium content, is known to vary over time, possibly reflecting interior dynamics. For example, the titanium content of the PKT maria increases by a few percent around 2.3 Ga (Kato et al., 2017; Sato et al., 2017). This transition indicates a change in magma source composition, possibly related to a hot plume containing IBC material. In addition to the currently exposed mare, several works have identified ancient basalt covered with highland regolith, the so-called cryptomare (e.g., Giguere et al., 2003; Izquierdo et al., 2024; Whitten & Head, 2015a, 2015b). Spectral comparison between cryptomare and lunar regolith samples has shown that low-titanium basalt matches ancient cryptomare basalts the most closely (Whitten & Head, 2015a). The surface age of the cryptomare region suggests that the cryptomare emplacement occurred before 3.8 Ga (Whitten & Head, 2015b). This timeframe overlaps with the period of the lunar expansion; however, the distribution of cryptomaria does not correspond with the distribution of expansion-related magmatism, as observed in the gravity data. Therefore, in order to gain a deeper understanding of mantle evolution during the expansion phase, it is necessary to obtain compositional constraints on magmatism directly related to the ancient expansion, which may be invisible in the surficial data alone.

To gain insights into the geologic features associated with the chronology and composition of the expansion-related magmatism, regions above lunar linear gravity anomalies (LGAs) are of particular interest. The NASA Gravity Recovery and Interior Laboratory (GRAIL) mission collected high-resolution lunar gravity data (Zuber et al., 2013), enabling the identification of linear positive Bouguer anomalies with lengths of over one hundred kilometers (Andrews-Hanna et al., 2013). Given their narrow and long geometries, LGAs have been interpreted as ancient vertical tabular intrusions or dikes exhibiting a higher density than the surrounding crust. The random orientations of LGAs on both the near and farsides suggest that LGAs were formed under a globally isotropic extension of the lithosphere (Andrews-Hanna et al., 2013). Moreover, Sawada et al. (2016) have revealed that LGAs overlap topographic depressions, similarly indicating horizontal tensile stress during the LGA formation. The composition of the LGA intrusion remains poorly understood. While some LGAs have been identified in the vicinity of surface mare (e.g., Panwar et al., 2023), compositional constraints remain limited due to the lack of connection between these anomalies and surface volcanic rocks.

We emphasize that highland areas covering LGAs and superposing craters are optimal locations to find evidence of ancient magmatism. Some LGAs are superposed by large craters, such as Rowland crater on LGA1 (Figures 1a and 1b), Roche crater on LGA2 (Figures 1c and 1d), Crisium basin on LGA4, and Edison crater on LGA20 (Figures 1e and 1f). Note that the LGAs are numbered in the same way as Andrews-Hanna et al. (2013) and Sawada et al. (2016). Based on the previous estimation of LGA structures, the top depth of intrusions could be about 10 km in the shallowest case (Liang & Andrews-Hanna, 2022). It can be surmised that these craters may have excavated a proportion of the LGA materials if they were younger than LGA. The calcium content of pyroxene can distinguish such LGA ejecta. LGA material originating from a partially molten region in the mantle presumably contains high-calcium pyroxenes (HCP) because the melting temperature of HCP is lower than that of low-calcium pyroxene (LCP) (e.g., Dasgupta et al., 2007). In addition, the surface maria and gabbroic pluton on the Moon are composed of HCP-bearing rocks (e.g., Lucey & Hawke, 1988), supporting our presumption of an HCP-rich LGA. Moreover, the recent thermal models predict that the lunar expansion phase may have persisted for a longer period than the LCP-rich Mg-suite magmatism (Laneuville et al., 2013; U et al., 2022; N. Zhang et al., 2013a, 2013b). The formation age of Mg-suite samples has been constrained to a short range around approximately 4.3 Ga, while the chronology of HCP-containing basaltic samples ranges in a longer period from



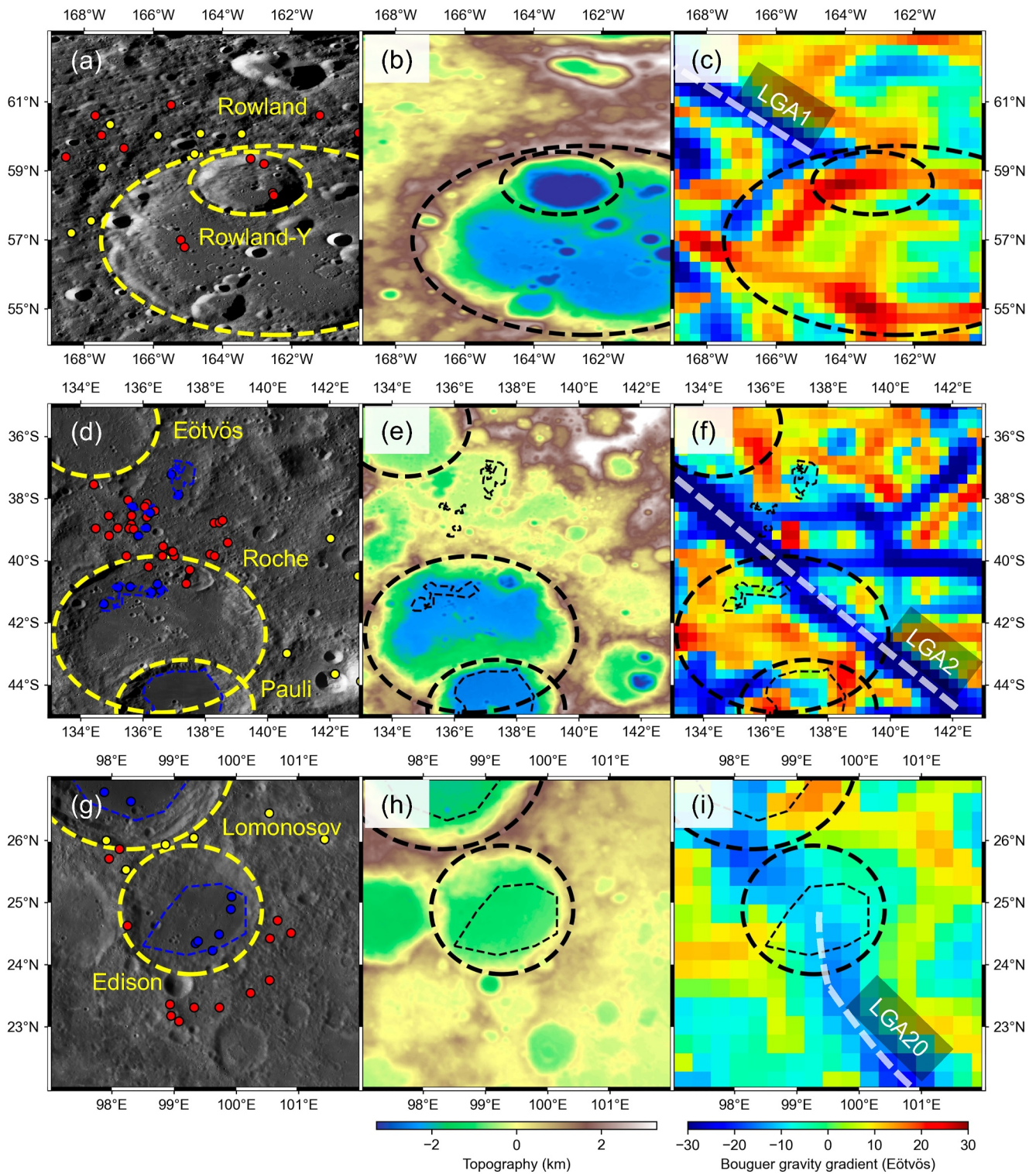


**Figure 1.** LRO WAC images (a, d, g; Speyerer et al., 2011), Global Lunar DTM 100 m topographic model GLD100 (b, e, h; Scholten et al., 2012), and Gravity Recovery and Interior Laboratory gravity gradient maps (c, f, i) of regions analyzed in this paper. Crater rims are shown in the yellow and black lines on the reflectance and gravity gradient maps, respectively. Small maria are shown as the blue and black lines on the WAC, topography, and gravity gradient maps, respectively. The red, blue, and yellow points on the WAC maps show the locations of fresh exposures labeled as E, M, and H in Table S2. The LGAs are traced with white dashed lines on the gravity gradient maps. (a–c) Rowland crater and LGA1. LGA1 seems to terminate around the rim of Rowland crater. (d–f) Roche crater and LGA2. LGA2 crosses the Roche crater. This region possesses small maria (Pasckert et al., 2015). (g–i) Edison crater and LGA20. LGA20 seems to cross the Edison crater.

4.35 to 2.03 Ga (e.g., Li et al., 2021; Terada et al., 2007). We revisit this presumption later to consider the possibility of LCP-bearing LGA intrusion in the view of the LGA chronology (see Section 5). The similarity of pyroxene calcium abundance between mare and LGA intrusions may prevent the identification of excavated intrusions around the Crisium basin, which is covered with mare basalts. On the other hand, the spectra of highland regions are dominated by LCP, which exhibits distinct absorption features compared to HCP (Cloutis & Gaffey, 1991; Denevi et al., 2007; Klima et al., 2007, 2011; Lucey et al., 2014; Ogawa et al., 2011; Yamamoto et al., 2015). It can thus be hypothesized that if highland craters (Rowland, Roche, and Edison) excavated LGA materials, distinguishable spectra of exposures might be found in the peripheries of those craters. Such exposures would allow us to look into the LGA composition. Note that only three craters, Rowland, Roche, and Edison, meet the criteria and are involved in this analysis. The rim-to-rim diameters and central coordinates of these craters are summarized in Table S1 and Figure S1 in Supporting Information S1. By integrating the chronological information of the craters and the cross-cutting relationships between these LGAs and craters, the age of the LGA formation could also be constrained by the presence of excavated materials.

To investigate the composition of ancient magmatism and the chronology of the initial lunar expansion, this paper analyzes the geology around Rowland, Roche, and Edison craters in terms of the LGA material and history. We first show the spectral features in the continuous ejecta region of these craters. By identifying the HCP-containing exposures in reflectance data sets, we ascertain whether each region contains potential basaltic LGA-containing exposures. Further, we estimate the FeO and TiO<sub>2</sub> contents of the identified candidates as indicators of the LGA composition. Although subsequent regolith mixing and space weathering weaken the spectral absorption by HCP, fresh materials particularly exposed at small new craters and steep slopes may exhibit distinctive spectra for identification. Then, we investigate whether these exposures originated from the LGA material or not. Later in this paper, we simulate deformation and excavation during the cratering process to compare with the gravity observation and confirm the possibility of such an excavation scenario. Finally, we propose the compositional properties of ancient magma sources and discuss the ancient lunar magmatic and thermal evolution. The potential titanium content of the LGA material is of particular interest, as it may provide insights into the IBC-related evolution of the mantle.

## 2. Spectral Analysis Method

To identify probable ancient magma exposures, we analyzed spectral data sets obtained from previous lunar missions in two steps. First, we made a compositional map within the targeted area using the Multiband Imager (MI) data taken by the Japanese lunar orbiter Kaguya (Ohtake et al., 2008). MI has the advantage of mapping the material distribution with a high spatial resolution, but it remains challenging to distinguish between LCP and HCP from MI, whose spectral resolution is not sufficient to determine 1,000- and 2,000-nm absorption centers of pyroxenes. Therefore, we conducted a supplementary analysis of the hyperspectral data from the Moon Mineralogy Mapper (M<sup>3</sup>) onboard the Chandrayaan-1 spacecraft.

### 2.1. MI Map Data Analysis

Our analysis used the MI\_MAP products that include mosaics of reflectance at nine bands spanning the visible to near-infrared wavelengths. The MI camera is equipped with five visible (415, 750, 900, 950, and 1,000 nm) and four near-infrared (1,000, 1,050, 1,250, and 1,550 nm) bands. The published MI\_MAP products have already been normalized by a photometric function with local topography and corrected via a reflectance comparison between the Apollo-16 sampling site and a lunar soil sample (Ohtake et al., 2008, 2013; Yokota et al., 2011). The spatial resolution of MI\_MAP is 2,048 pixels/degree, corresponding to 15 m/pixel at the equator. To minimize potential errors originating from a steep slope or surface roughness (Ohtake et al., 2013), the MI data were binned into 4 × 4 pixel bins. Also, some values are unreasonably negative due to shadows cast by steep terrain features such as crater walls. Accordingly, we excluded these pixels from the binning process and subsequent analysis.

Searching for fresh basaltic materials, we made an RGB color composite map of spectral absorption depths (Ohtake et al., 2014; Taguchi et al., 2017) (Figure 2a). First, we normalized the spectrum by a continuum between 750 and 1,550 nm at each binned pixel and mapped the absorption depths from the continuum at 950, 1,050, and 1,250 nm. Then, we composited these three maps as RGB (red: 950 nm; green: 1,050 nm; blue: 1,250 nm). The spectral depressions denoting olivine and pyroxene, which comprise lunar basalts, are displayed with whiter colors. Conversely, anorthosite exposure appears blue due to a lack of absorption at the 950- and 1,050-nm bands.



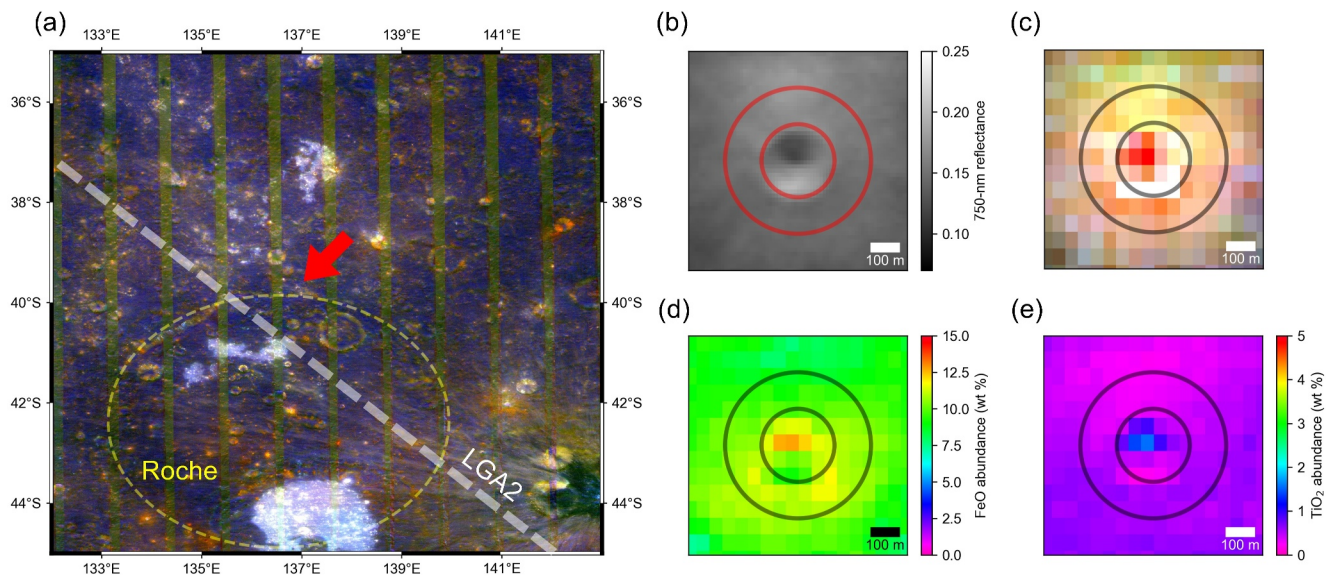


**Figure 2.** (a) RGB composite map around LGA2. (b–e) Maps of 750-nm reflectance, RGB composite, FeO abundance, and TiO<sub>2</sub> abundance at E1 (indicated by the red arrow in (a)). The red or black lines show circles with one and two radii of the fresh crater whose inside is filled with basaltic material. Note that the images except for (b) are binned by 4 × 4 pixels.

In addition, space weathering on the Moon generally weakens the absorption features of minerals; thus, fresh materials are brighter on the map.

We next identified candidates of basaltic exposures from the composite map by visual inspections and categorized them morphologically (Figure 2b). In comparison with the topography from SLDEM2015 (Barker et al., 2016), we chose basaltic white spots on the RGB-composite map (Figure 2c). The selected white spots generally have absorption depths of more than 8% at 950- and 1,050-nm bands, and 3% at 1,250-nm band. The fresh material is generally exposed around new craters or at steep slopes, so we attached flags, such as “crater” or “slope,” to the identified locations, depending on their morphologies. Examples of geomorphology of the exposure candidates are also shown in Figure S2 in Supporting Information S1. It should be noted that white spots in topographically low areas are excluded because these sites might represent small maria (Figure S3 in Supporting Information S1). As endmember spectra for the latter analysis, we also extracted data in both highland and mare that exhibit high Optical Maturity Parameter (OMAT) values and, therefore, are fresh (Lucey, Blewett, & Jolliff, 2000; Lucey, Blewett, Taylor, & Hawke, 2000).

Finally, we characterized the compositions around the candidates. From empirical algorithms deriving iron and titanium contents from MI reflectance ratios (Lucey, Blewett, & Jolliff, 2000; Lucey, Blewett, Taylor, & Hawke, 2000; Otake et al., 2012), FeO and TiO<sub>2</sub> distributions were calculated. We then estimated their average and standard deviation for each location. At exposures on slopes, we manually fitted a circle on white pixels and simply averaged the values. In the case of craters, we averaged values outside a circle fitted to the crater rim, as shown in Figures 2d and 2e. Depending on the illumination conditions, reflectance values occasionally become unrealistic within craters, making iron and titanium contents too high or low. For example, Figures 2d and 2e show anomalously high FeO and TiO<sub>2</sub> abundances in the E1 crater, which are attributed to the shadow cast by the north-western wall of the crater (Figure 2b). To avoid significant errors due to these problems, we calculated the azimuthal average and standard deviation of area 1–2 crater radii away from its center. This region is covered by continuous ejecta (Melosh, 1989; Moore et al., 1974), which allows us to treat it as a representative value of materials exposed by the fresh crater.

## 2.2. M<sup>3</sup> Data Analysis

We analyzed hyperspectral reflectance around the candidates using the M<sup>3</sup> L2 products (Malaret, 2011). M<sup>3</sup> was an imaging spectrometer that obtained cube images composed of two spatial and one spectral dimension. M<sup>3</sup> covered wavelengths approximately from 400 to 3,000 nm with spatial resolutions of 70–140 and 140–280 m/pixel for

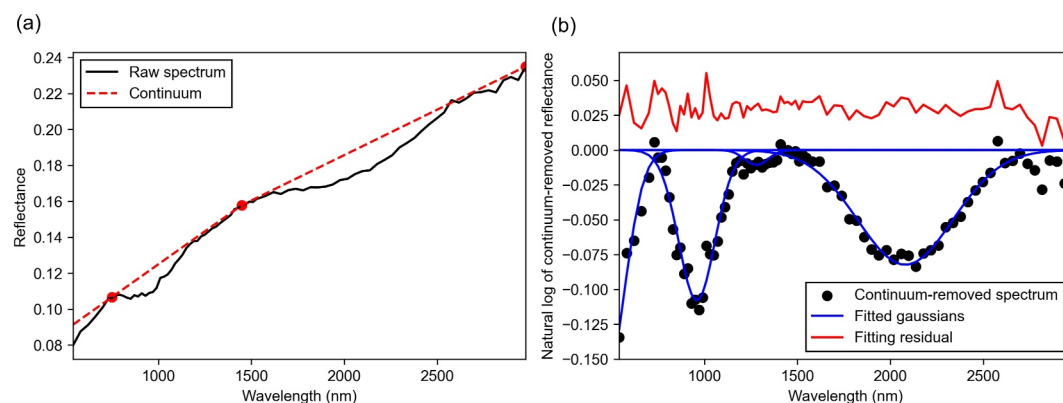


**Figure 3.** Example of spectral analysis routine for  $M^3$  data set. (a) One of the spectra at LGA2-E1 from the image of M3G20090529T060422. The spectrum after all the calibration is shown in black. The red points correspond to tie points used for a two-part linear continuum generation shown as the red dashed line. (b) Demonstration of our modified Gaussian model deconvolution. The black dots are the natural log of reflectance values normalized by the continuum. The blue lines are four Gaussian fitted to the continuum-removed reflectance. The fitting residual is shown in red with an offset of 0.03.

Target and Global modes, depending on the spacecraft altitude (Green et al., 2011; Pieters et al., 2009). The reflectance data have been published as the L2 products after solar irradiance correction, statistical polishing, removal of thermal emission, and photometric correction (Besse et al., 2013; Boardman et al., 2011; Clark et al., 2011; Green et al., 2011; Isaacson et al., 2013). It should be noted that the ground truth correction is not applied to the L2 product, but the correction factor derived from the average 62231 soil is also published in the  $M^3$  data archive. It is well known that this correction improves the characterization of the 1,000-nm absorption position on highland soil (Isaacson et al., 2013). The correction factor depends on  $M^3$  optical periods because a wide range of the detector temperature due to the solar zenith angle generates artifacts in the acquired spectra (Isaacson et al., 2013). Therefore, we applied the correction factors of the corresponding optical periods to each L2 product in the subsequent analysis.

Prior to the determination of pyroxene type at each location, a continuum was subtracted from the corrected reflectance in the same manner as Whitten and Head (2015a). As a consequence of space weathering, lunar spectra have a red-sloped continuum. To obtain accurate mineralogical absorption, this effect has been removed in previous lunar hyperspectral characterization (e.g., Isaacson et al., 2011; Sunshine et al., 1990; Yamamoto & Watanabe, 2021; Yamamoto et al., 2018). To remove the aforementioned continuum, our analysis employed the convex hull method that finds a polygonal line connecting three tie points (Figure 3a). The first tie point was set at 750 nm, but the second and third were able to vary in the wavelength range of 1,329–1,778 nm and beyond 2,776 nm, respectively. The second and third tie points were selected so that the polygonal line among the three tie points did not intersect with the  $M^3$  spectrum. Finally, the spectrum was divided by this two-part linear continuum, and the band depth at each wavelength was calculated.

To identify the pyroxene type, the modified Gaussian model (MGM) was then applied to the continuum-removed spectra (Figure 3b). MGM has been demonstrated to be a robust algorithm to characterize pyroxene spectra in visible to near-infrared wavelengths (e.g., Denevi et al., 2007; Sunshine et al., 1990). This approach allows for the deconvolution of the spectra into multiple Gaussian. The central wavelengths of the deconvoluted Gaussian are significant indicators of pyroxene compositions. Based on previous reflectance analysis on natural and synthetic pyroxenes (Denevi et al., 2007; Klima et al., 2007, 2011), Gaussian centered at 900–1,000 and 1,800–2,400 nm have their peaks at shorter wavelengths for LCP and vice versa for HCP. Additionally, HCP has an absorption at 1,300 nm, although LCP exhibits no absorption there. Therefore, our analysis fitted four Gaussian to the spectra by setting the initial centers of Gaussian at 300, 1,000, 1,300, and 2,000 nm, following Ogawa et al. (2011). The calculated band positions were finally compared with those of synthetic and natural LCP and HCP (Denevi et al., 2007; Klima et al., 2007, 2011). To avoid noisy spectral data in the latter discussion, only exposures with a maximum absorption depth at 900–1,000 nm larger than 10% and root-mean-square of fitting residual less than 0.02 were chosen. These restrictions on the signal-to-noise ratio in our  $M^3$  analysis, therefore, reduced the number of analyzed exposures from that in the MI data analysis.

### 3. Spectral Features Around LGAs

#### 3.1. LGA1

The RGB-composite map revealed the presence of white spots around Rowland crater; however, the number of locations with white colors is much less than that around LGA2 (Figures S4 and S5 in Supporting Information S1). We identified 13 pyroxene-rich exposure candidates inside and outside the Rowland crater in total and labeled them with a mark of exposure (E) and an ID number. Note that the spots inside Rowland were included in the analysis, too, because magmatic material could have been mixed within the crater during its formation. For comparison, we also extracted eight anorthositic spots on the composite map as typical highland materials. It should be noted that no maria exists in this region (Figure 1a). The longitude and latitude of each location are provided in Table S2.

The MI data around LGA1 revealed almost no signs of significantly elevated FeO and TiO<sub>2</sub> abundances. The MI data of this region commonly exhibit FeO and TiO<sub>2</sub> abundances below 4 wt.% and 1 wt.%, respectively (Figure S4 in Supporting Information S1). On the FeO map around Rowland crater, no obvious anomaly can be seen at the north-western part of the crater, where the LGA ejecta are hypothesized to be distributed. The FeO and TiO<sub>2</sub> abundances at the exposures show the same tendency as other areas in Figure 4a. Except for a few candidates, such as E3, FeO abundance in these exposures is 8 wt. % at most, which is approximately half of that in typical maria (Figures 4c and 4e). These values are included in the range of noritic materials (Lucey et al., 1998), which is thought to be a typical rock type of the lunar lower crust.

The M<sup>3</sup> spectral features indicate that the pyroxene characteristic in this region is similar to LCP. Figure 4b compares the absorption peak positions at the 1,000- and 2,000-nm bands to laboratory LCP data. Owing to the low signal-to-noise ratio and weak absorption in the M<sup>3</sup> data of this region, the number of candidates was limited. Nevertheless, the calculated 2,000-nm peak positions were always shorter than 2,100 nm, ranging similarly to the synthetic LCP data. LCP is known to be dominant on the spectra of noritic rocks. It is noteworthy that all candidates near Rowland crater exhibit LCP-like spectra even though we extracted the exposures with the FeO contents higher than the typical value in this region (Figure S7 in Supporting Information S1). Therefore, these pyroxene exposures around LGA1 can be interpreted as materials ejected from the noritic lower crust, not from basaltic magma intrusions comprising HCP.

#### 3.2. LGA2

From the MI composite map around LGA2, we identified 29 white exposures in the northern area of Roche crater. This distribution is consistent with that of the FeO distribution in the vicinity of Roche crater (Figure S5 in Supporting Information S1). Because Roche crater is superposed by Pauli crater (Figure 1), the southern part of this area is excluded conservatively in this study. Furthermore, the eastern side of Roche is not analyzed because of contamination by bright ejecta rays originating from the Eratosthenian-aged Ryder crater.

It is noteworthy that this region contains small maria between the Eötvös and Roche craters (Figure 1). Pasckert et al. (2015) and Wilhelms and El-Baz (1977) have already identified young mare patches inside Roche and Pauli craters. A comparison between the composite and topography map has identified four additional candidates of mare patches in the northern part of Roche (Figure S3 in Supporting Information S1). The composite color of these candidates appears white in a topographically low area, indicating that basaltic materials are confined to topographic depressions. They were considered basalts that erupted in the same way as nearby maria, and hence, we carefully excluded these areas from our exposure identification process. These locations were included as mare exposures (marked with M and ID number) and compared to other pyroxene exposures later. Given that impact melt often forms a pond in a topographically low area, this procedure effectively eliminates impact melt.

The FeO contents of the pyroxene exposures are probably a mixture of mare-like and highland materials in this studied region. As shown in Figure 4c, the candidates are distributed continuously between highland and mare materials of this region. Some of their FeO contents exceed even 12 wt. % and are higher than those of noritic lunar rocks (Lucey et al., 1998). However, the values are slightly lower than that of maria. Similarly, the TiO<sub>2</sub> contents range from 0.5 to 1.3 wt. %, exhibiting variation between mare and highland materials. Therefore, the compositional characteristics of these pyroxene-like exposures indicate a mixture of highland anorthosite and mare-like basaltic material.

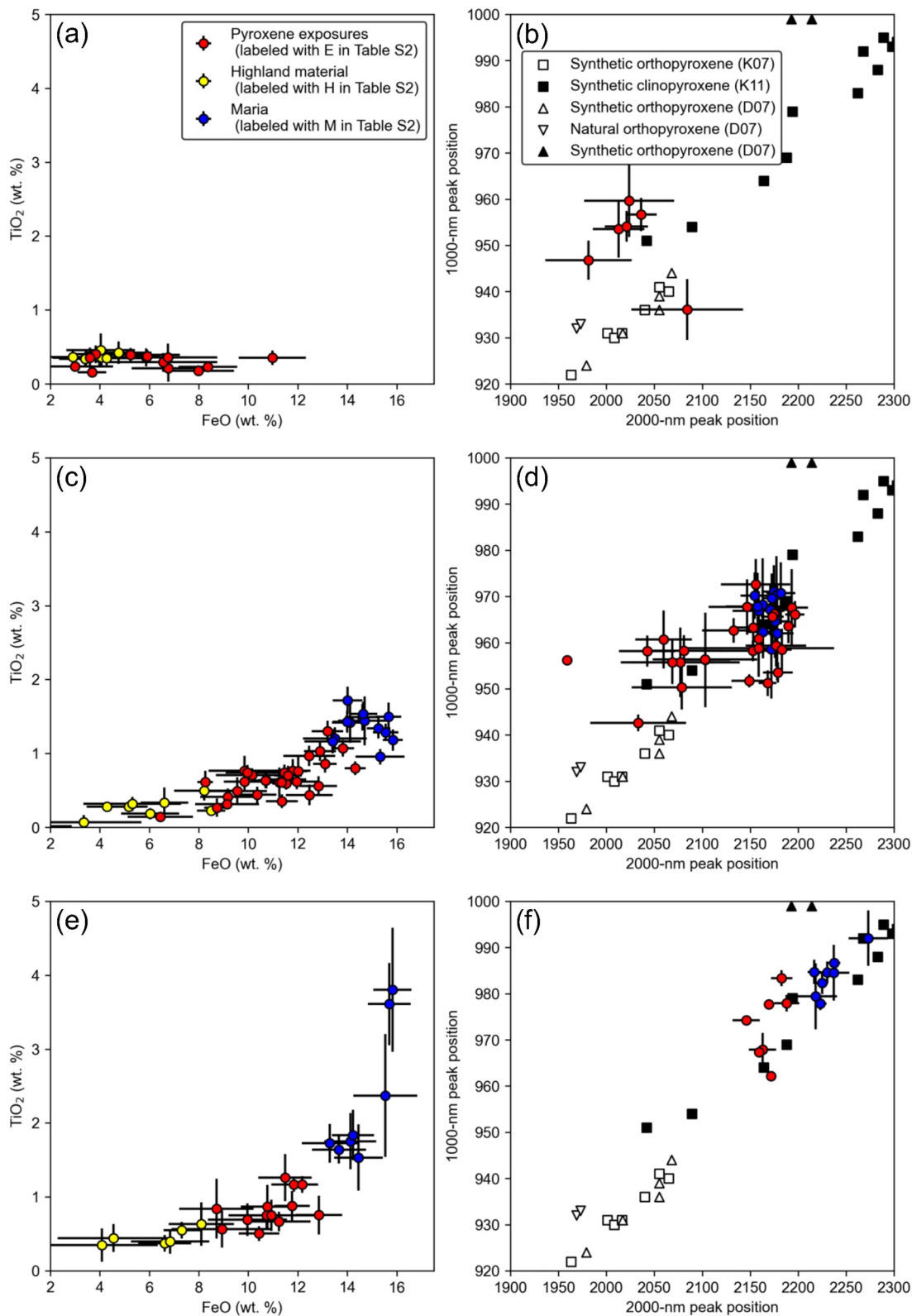


Figure 4.



The absorption peaks provide additional evidence that the surface regolith around LGA2 contains a mixture of basaltic material. In Figure 4d, the majority of both 1,000- and 2,000-nm peak positions are distributed outside the LCP range but within a range comparable to HCP. While both 1,000- and 2,000-nm peak wavelengths are shorter than those of the majority of synthetic clinopyroxene (HCP) and some of them are similar to LCP, the majority of the pyroxene exposures overlap with maria materials. Furthermore, many of them exhibit peak positions that are nearly identical to those observed in the maria in this region, indicating a mixture of basaltic materials as evidenced by the FeO and TiO<sub>2</sub> trends.

### 3.3. LGA20

There exist bright exposures in the composite map near LGA20, particularly in the southern region of its center, and we identified 13 candidates in total. The areas inside Edison and Lomonosov craters are covered by maria (Figure 1), so we selected eight fresh craters in the mare area as reference points for basalt.

The FeO and TiO<sub>2</sub> contents are continuously distributed between mare and highland materials, exhibiting a pattern similar to that observed in LGA2. As shown in Figure S6 in Supporting Information S1, the mean FeO content around LGA20 ranges from 8 to 10 wt. %, which is much higher than that of the typical highland. Some locations near the rim of the Edison crater exhibit FeO of 10% or above. The variation of TiO<sub>2</sub> content is also similar to that observed around LGA2 and stays within the range of 0.5–1.5 wt. %. In contrast, the TiO<sub>2</sub> content in the mare area is more widespread than that observed around LGA2. This is likely due to the higher abundance of TiO<sub>2</sub> in the mare within Lomonosov crater (see Figure S6 in Supporting Information S1), which may be attributed to either a temporal change in magma composition in this region or a contamination of Edison's mare by low-FeO highland material (Giguere et al., 2003).

The 1,000- and 2,000-nm pyroxene absorption peaks also indicate the presence of HCP around the Edison crater. The discovered pyroxene exposures exhibit absorption peaks in the range of clinopyroxene (Figure 4f). The main difference from LGA2 is that the peak wavelengths are a little shorter than those of mare. This could be due to a different extent of contamination by numerous highland ejecta or a compositional difference between maria and pyroxene exposures. The contamination by LCP-rich highland regolith possibly shifts the absorption centers of HCP exposures to a shorter wavelength. In addition, Roche and Edison craters are Nectarian and Pre-Nectarian aged, respectively (Öhman, 2015; Wilhelms, 1987; Wilhelms & Byrne, 2009), and the excavation event by Roche crater postdates that by Edison. Giguere et al. (2003) pointed out that the albedo of the mare inside Edison crater is higher than that of other maria possibly due to the deposition of highland ejecta. Thus, the contamination of highland material is potentially more enhanced around LGA20 than around LGA2.

### 3.4. Possible Sources of Discovered Basaltic Exposures

Our spectral analysis shows that the peripheries of LGA 2 and 20 possess exposures with high FeO and HCP-like absorptions. The number of analyzed spots is limited because exposures fresh enough for the spectral analysis are rare; however, we selected the most probable spots as basaltic material. Even at the analyzed spots with FeO higher than the average (Figure S7 in Supporting Information S1), the pyroxene absorption features at LGA2 and 20 are different from those at LGA1. This difference is consistent with ejecta deposition suggested by the FeO distribution around the craters (Figures S4b, S5b, and S6b in Supporting Information S1), indicating that the basaltic spots around LGA2 and 20 are related to a process that LGA1 has not experienced. As a potential scenario, we propose the ancient excavation of basaltic LGA materials by Roche and Edison craters. However, this observation might also be attributed to other causes: ejecta from a mare, impact melt, pyroclastic material, and mafic melt trapped within the crust during the magma ocean solidification.

The first possibility of basaltic ejecta from mare regions is likely excluded based on ejecta distribution modeling. Within the regions covering basaltic exposures exist some small maria that also have HCP and a high FeO

**Figure 4.** Compositional summary of the spectral analysis results of the Multiband Imager and M<sup>3</sup> data sets. Results are summarized for each region: (a, b) around LGA1, (c, d) around LGA2, and (e, f) around LGA20. The red and blue points correspond to pyroxene exposures on the highlands and maria labeled with E and M, respectively. The yellow points are highland material exposures. (a, c, e) FeO and TiO<sub>2</sub> abundance at each location. The error bar is a standard deviation of all the values within the spots. (b, d, f) 1,000- and 2,000-nm absorption peak positions at exposure candidates. The error bar is the standard deviation of the M3 pixels of those candidates. The black squares and triangles are synthetic clinopyroxene (high-calcium pyroxenes) data from Denevi et al. (2007) and Klima et al. (2011), respectively. The white squares and triangles are synthetic and natural orthopyroxene (low-calcium pyroxene) data from Denevi et al. (2007) and Klima et al. (2007), respectively.

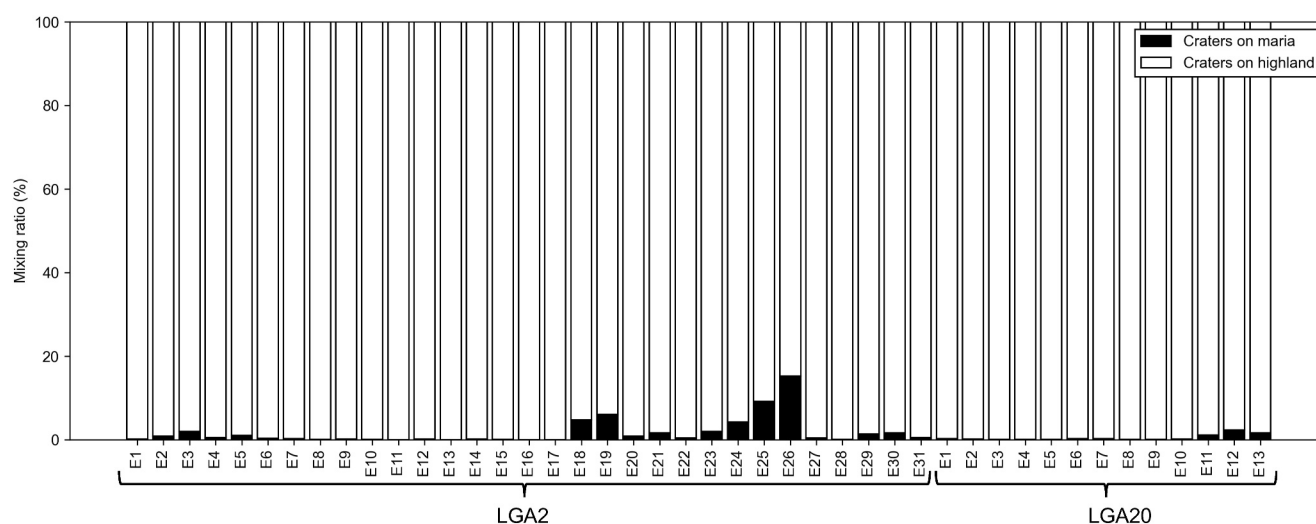


**Figure 5.** The ratio of ejecta deposited at each high-calcium pyroxenes exposure was around LGA2 and 20. The black and white boxes show the contribution of ejecta from craters on mare and highlands, respectively.

abundance. The HCP exposures could be caused by the deposition of basaltic mare material ejected from the nearby small maria after the Roche/Edison formation. To model this effect, we integrate the empirical relationship between ejecta thickness and distance from a crater (McGetchin et al., 1973; Melosh, 1989) with one of the global lists of craters with a diameter of 1 km or larger (Wang et al., 2021). In this estimation, craters smaller than Roche/Edison are considered because they tend to be younger than the Roche/Edison formation. Figure 5 shows the ratio of ejecta from mare regions (thin dashed lines in Figure 1). Our modeling suggests that the ejecta deposited on the pyroxene candidates is predominantly composed of highland ejecta and that the ratio of ejecta from mare craters is consistently lower than 10 wt. %. Such low mixing ratio results in the FeO contents being as low as highland material and inconsistent with the observed values. For instance, application of a spectrum of 10% HCP and 90% plagioclase mixture (Yamamoto et al., 2015) to the empirical algorithm (Otake et al., 2012) yields a FeO abundance as low as 0 wt. %. Although this algorithm is not calibrated for such a low-FeO material, this application result suggests that the mare ejecta contamination of 10% does not account for the high-FeO and HCP exposures around LGA2 and 20. While crater rays have the potential to transport ejecta much farther from the source craters than continuous ejecta, their spatial compactness makes quantitative evaluation difficult.

The impact melt is also unlikely to be the source of these exposures. Once a crater-forming impact occurs, this energetic event melts the target material. Previous remote-sensing data of impact melt have demonstrated absorption peaks consistent with HCP (e.g., Moriarty & Pieters, 2018). In contrast, impact melt can be distinguished from the pyroxene exposures using topography captured by the Narrow Angle Camera onboard the Lunar Reconnaissance Orbiter (Robinson et al., 2010). Impact melt often forms pond-like morphology; therefore, topographic depressions filled with basaltic spectra on the RGB map are excluded from the exposure candidates as described above (Figure S3 in Supporting Information S1). Also, areas near the candidates do not exhibit the morphological elements specific to impact melt, such as flow features and cooling fractures (Figure S2 in Supporting Information S1), as seen in impact melt around other craters (e.g., Osinski et al., 2011). Topographic degradation could obscure the impact melt morphology at ancient ejecta from Roche; however, this scenario is unlikely to account for the spectral difference between Rowland and Roche, as the degradation levels are expected to be similar at these two craters that share a common size and age (Table S1 in Supporting Information S1, Wilhelms & El-Baz, 1977).

As the third possibility, the observed HCP exposures could be pyroclastic glasses emplaced by explosive volcanic eruptions, akin to the dark mantle deposits identified on the Moon (e.g., Besse et al., 2014). By using Clementine multispectral images, Giguere et al. (2003) categorize the southern region of Edison crater as dark mantle deposits of probable pyroclastic origin based on its low albedo. Such pyroclastic materials might exhibit moderately high FeO abundances in our estimation from multiband reflectance. This confusion arises because the empirical formula between reflectance and FeO is not calibrated for glasses, unreasonably enhancing the FeO abundance at

dark mantle deposits (Giguere et al., 2003; Otake et al., 2012). However, the peak positions of dark mantle deposits in the 1,000- and 2,000-nm bands appear at wavelengths above 990 nm and beyond 2,000 nm (e.g., Besse et al., 2014; Kumaresan & Saravanavel, 2022). Such peaks are distinguishable from the continuous distribution of pyroxene exposures shown in Figure 4.

The final alternative source is mafic melt trapped within the crust, which seems unlikely as well. Several studies on lunar hyperspectral data have identified HCP mixtures in highland craters, which could be attributed to mafic liquid trapped within the anorthositic cumulates during the lunar magma ocean solidification (Ogawa et al., 2011; Yamamoto et al., 2015). A numerical simulation by Piskorz and Stevenson (2014) also suggests that mafic melt may be trapped in the lunar crust shallower than 5 km during the formation of floating anorthosite cumulates. In contrast, a global survey of HCP by Yamamoto et al. (2015) shows that rayed craters accompanied by HCP have diameters of 10 km or larger and that no craters with diameters less than 6–10 km possess HCP. This result implies that the uppermost crustal layer within a depth of 1 km predominantly consists of LCP rather than HCP. The global survey of the 1,000-nm absorption center at fresh craters also shows that 99% of the highland craters smaller than 1 km have band minima consistent with LCP, supporting the dominance of LCP on the lunar highland (Lucey et al., 2014). To eliminate the possibility of the excavation of mafic melts at a depth below 1 km, our analysis focused on craters with diameters of 8 km at largest, and the majority of them are smaller than a few hundred meters. In addition, even if the Roche-forming impact excavated and ejected the trapped melt, the high FeO content at the discovered exposures (Figure 4) does not agree with this hypothesis. The fraction of trapped melt in the crust is expected to be lower than 20% (Piskorz & Stevenson, 2014), which would result in a FeO content below 4%.

In summary, the pyroxene exposures analyzed in our study are not likely to have originated from basaltic materials that currently exist on the lunar surface, either as maria or impact melt. In particular, the aforementioned hypotheses have difficulty explaining the difference in the existence of HCP exposures between the two craters of comparable size, Rowland and Roche. While all the hypotheses cannot be ruled out completely, it is worth testing the LGA excavation scenario as a potential origin for the observed exposures.

#### 4. LGA Excavation Indicated by Gravity Anomaly

As a possible hypothesis, the presence and absence of the HCP exposures around the Rowland, Roche, and Edison craters may be attributed to whether the subsurface LGA material was excavated by these craters or not. To test this hypothesis, we compare cratering simulation results and lunar gravity data. Interestingly, as seen in Figure 1, the linear structures in the lunar gravity gradient map have different characteristics inside craters; LGA1 appears terminated at the rim of Rowland crater (Liang & Andrews-Hanna, 2022; Figure S8a in Supporting Information S1), but LGA2 penetrates through the Roche crater (Andrews-Hanna et al., 2013; Figure S8b in Supporting Information S1). Both craters have similar diameters of around 160 km. Therefore, we simulate the subsurface modification and excavation by these craters and calculate variations of gravity anomalies after the crater formation to test the LGA excavation hypothesis.

Our gravity modeling consists of two parts: (a) estimation of possible subsurface structures from the GRAIL gravity data and (b) simulation of gravity change due to excavation and deformation of the subsurface structure by the crater formations. Due to the non-uniqueness of gravity inversion, a certain variety of subsurface structures satisfy the observed gravity data. Thus, a set of intrusion shapes is first prepared to reproduce gravity anomalies outside the featured crater, assuming that crustal deformation due to impact is negligible there. A variety of density differences between the intrusion and the surrounding crust are considered. Next, we simulate the post-impact gravity for the set of intrusion geometry. With the iSALE shock physics code (Amsden et al., 1980; Collins, 2014; Collins et al., 2004, 2011; Ivanov et al., 1997; Melosh et al., 1992; Wünnemann et al., 2006), we trace the subsurface modification and calculate the gravity above the crater interior after its formation. Finally, we compare the simulation and observed data, and discuss the cross-cutting relationship between LGAs and the craters.

##### 4.1. Modeling Procedure

We begin with the preprocessing of Bouguer gravity data around the craters by filtering specific wavelengths and rotating the coordinates. In the same manner as Andrews-Hanna et al. (2013), we first construct a band-passed Bouguer anomaly map. From a lunar Bouguer-corrected gravity model of GRGM1200A\_BOUGUER



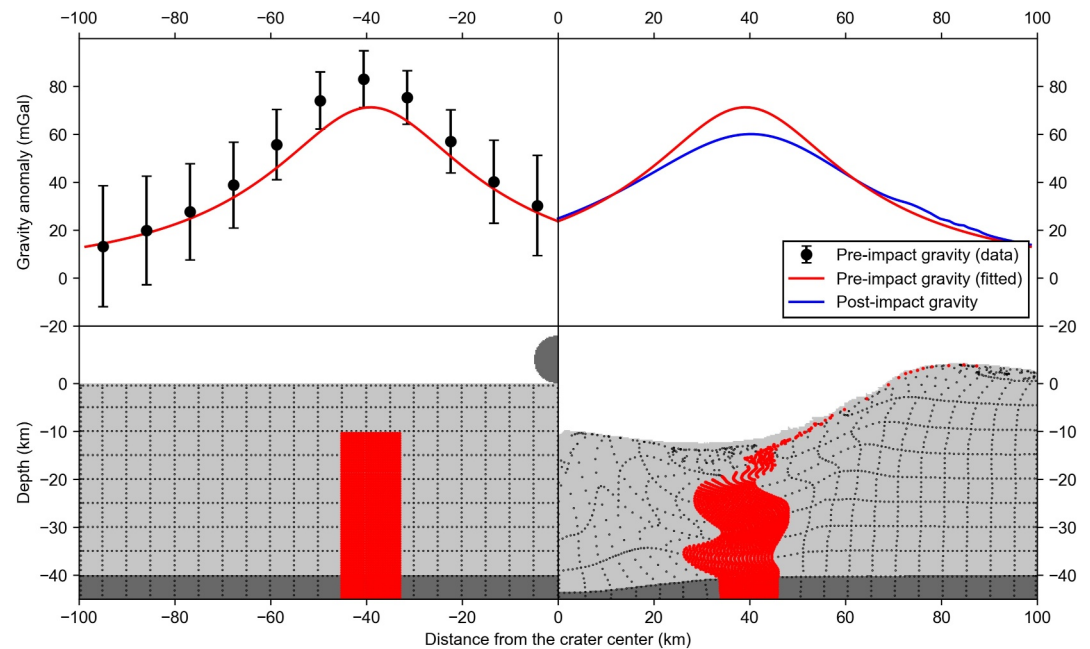


**Figure 6.** An example of our LGA modification simulation. The left and right figures show the results before and after cratering, respectively. The upper and bottom figures show the gravity profile perpendicular to LGA and the subsurface material distribution, respectively. The origin of the  $x$ -axis corresponds to the crater center. In the top-left figure, the gravity anomaly from a rectangular body (red line) is fitted to the averaged gravity profile (black points). In the bottom left figure, the corresponding rectangular intrusion is shown in red. The light and dark pixels are the crust and mantle. The dark semicircle in the bottom-left figure is the projectile. The blue line in the top right figure shows the gravity profile of the modified intrusion. The density difference and top depth assumed in this figure are  $400 \text{ kg/m}^3$  and  $10 \text{ km}$ , respectively.

(Lemoine et al., 2014), the spherical harmonic coefficients with degrees of 50–300 are extracted to filter out the noise effect and long-wavelength structures. The filtered gravity map was then rotated using spherical harmonic transformations so that LGA is located on the lunar equator. This allows us to apply a Cartesian coordinate in the subsequent analysis because the scale of interest is considerably smaller than the radius of curvature of the Moon (Liang & Andrews-Hanna, 2022).

Possible patterns of LGA structures before cratering are estimated by fitting a rectangular density anomaly to the gravity data outside the crater. The mean value of the LGA data outside the crater is considered to be representative of the typical pre-cratering gravity. It should be noted here that the gravity profile perpendicular to the LGA was averaged by aligning the peak gravity horizontally because the LGA is not completely straight. Then, the gravity values derived from an intrusive subsurface body with a uniform density were fitted to the averaged LGA profile. The density of the magma intrusion is as high as that of the mare basalt (Kiefer et al., 2012), but the source of gravity could be a swarm of dikes, which reduces the density difference rather than a single giant dike (Andrews-Hanna et al., 2013). Thus, the density difference between the intrusion and crust varies from 200 to  $1,000 \text{ kg/m}^3$ . Owing to the non-uniqueness of the gravity inversion, the shape of the intrusive body must also be assumed. In principle, the LGA value can be fitted by other complex shapes, such as T-like prisms, but Liang and Andrews-Hanna (2022) have revealed that changing the assumed shape does not significantly improve the fitting. Therefore, we assume the most straightforward tabular intrusion model hereafter, as Andrews-Hanna et al. (2013). A Bayesian approach by Andrews-Hanna et al. (2013) indicated that the probability of a top depth of less than  $5 \text{ km}$  is not zero. On the other hand, no mafic spectrum is observed just above the LGA, meaning that the LGA material does not reach the surface directly. Thus, a non-zero top depth was assigned at every  $2 \text{ km}$  interval. Then, with the assumed density and top depth of a tabular intrusion, its width and center position are treated as fitting parameters (Figure 6). It should also be noted that the root of the intrusion is located at the Moho boundary. Because magma is negatively buoyant above the lunar Moho, it is difficult to stall the dike without any pressure from magma in the mantle (Wilson & Head, 2017).

The subsurface material movements resulting from a meteoroid collision were numerically traced using a crater-forming simulation. In this study, we employed the iSALE-2D shock physics code (Amsden et al., 1980; Wünnemann et al., 2006, 2016; Zhu et al., 2015), which is based on the SALE hydrocode solution algorithm (Amsden et al., 1980). To simulate hypervelocity impact processes in solid materials, SALE was modified to include an elastoplastic constitutive model, fragmentation models, various equations of state, and multiple materials (Ivanov et al., 1997; Melosh et al., 1992). More recent improvements include a modified strength model (Collins et al., 2004), a porosity compaction model (Collins et al., 2011; Wünnemann et al., 2006), and a dilatancy model (Collins, 2014). In our simulation, a dunite projectile with a radius of 5 km collided with the lunar surface at a speed of 20.9 km/s. This impact speed was identical to the median speed of an asteroid collision with the Moon during the Late Heavy Bombardment epoch (Bottke et al., 2012). The target was assumed to be a two-layered surface composed of granite crust and dunite mantle. As a consequence, a crater with a diameter of 160 km was formed in our simulation. All the parameters are summarized in Tables S3 and S4 in Supporting Information S1. In addition, it should be noted that the selection of material parameters does not make a substantial difference (Text S1 in Supporting Information S1), as reported by previous studies (Melosh et al., 2013; Miljković et al., 2015).

The gravity anomalies before and after the collision were calculated by integrating the positions of the iSALE tracers, assuming that the subsurface structures of LGA continued both outside and inside the crater before its formation. Because our cratering simulation is axisymmetric, we trace the deformation of the rectangular LGA body within numerous radial and vertical cross-sections. Based on the simulated movement of the iSALE tracers, the deformation is calculated within a cross-section from the crater center at every azimuth angle. A map of the gravity anomaly subsequent to the impact is generated by transforming the post-impact positions of the LGA tracers to the three-dimensional coordinates and integrating their gravity. After the crater formation, the gravity value within 15 km from the intrusion center was reduced by 30 mGal at most, as demonstrated in Figure 6. Thus, we focused on the gravity within this narrow region inside the crater. Note that our simulation treats the crust as homogeneous because the gravity change due to the subsurface modification can be estimated by the use of the iSALE tracers alone. Although the density gap between the LGA intrusion and surrounding crust causes the reflection of shock waves and could suppress the modification beneath the crust, we confirmed that such a density gap has little influence on the overall comparison. Even when the density gap is set to be greater than  $800 \text{ kg/m}^3$ , the discrepancy in the resultant gravity between homogeneous and heterogeneous crust models is less than 5 mGal (Figure S9 in Supporting Information S1).

The gravity inside craters is additionally affected by the porosity alteration during the crater formation. Soderblom et al. (2015) showed that the Bouguer anomaly of lunar complex craters has a negative value on average, implying that the porosity beneath the crater is higher than the crust due to the fracturing by shock waves. Their analysis also reveals that the average gravity inside the crater has a significant variation among craters, ranging from +10 to  $-40 \text{ mGal}$ . These wide-spreading values are attributed to a variation in the pre-impact porosity beneath the crater because the impact can also close pores inside highly fractured material (Milbury et al., 2015). In addition, the gravity anomaly could be variable inside the crater. For example, if the initial porosity is high, pore closure is enhanced more in the central region of the crater than in the outer area, resulting in a high Bouguer anomaly around the crater center. This could affect the gravity profile in our analysis, especially in the case of LGA1, which is nearly radial to the center of Rowland crater. To incorporate these pore creation and destruction into our simulation, we included the dilatancy model to consider a variety of the initial porosity effect, following the parameters presented by Collins (2014), Milbury et al. (2015), and Miljković et al. (2021) (Table S3 in Supporting Information S1). The LGA gravity inside the crater is weaker than that outside for both Rowland and Roche craters, suggesting that the initial porosity was low. As demonstrated by Milbury et al. (2015), an initial porosity of 6.8% results in positive gravity values inside a 160-km-sized crater. Thus, we set the initial porosity for various values from 0% to 8%. Although Huang et al. (2022) suggested a lunar initial porosity as high as 10%, we employed a value below 8% to reproduce the gravity anomaly inside the crater that is lower than that of the surroundings. Such a decrease of gravity anomaly is commonly observed at Rowland and Roche craters. Next, we combined the gravity profiles from various porosity changes with the those from the LGA modification. After binning the simulated gravity distribution to the same resolution as the gravity data, we then identified the best-fit dilatancy model to minimize the residuals of our simulation from the data. For this comparison, pixels located inside the crater and within 10 km of the LGA center were considered corresponding to the area where gravity is

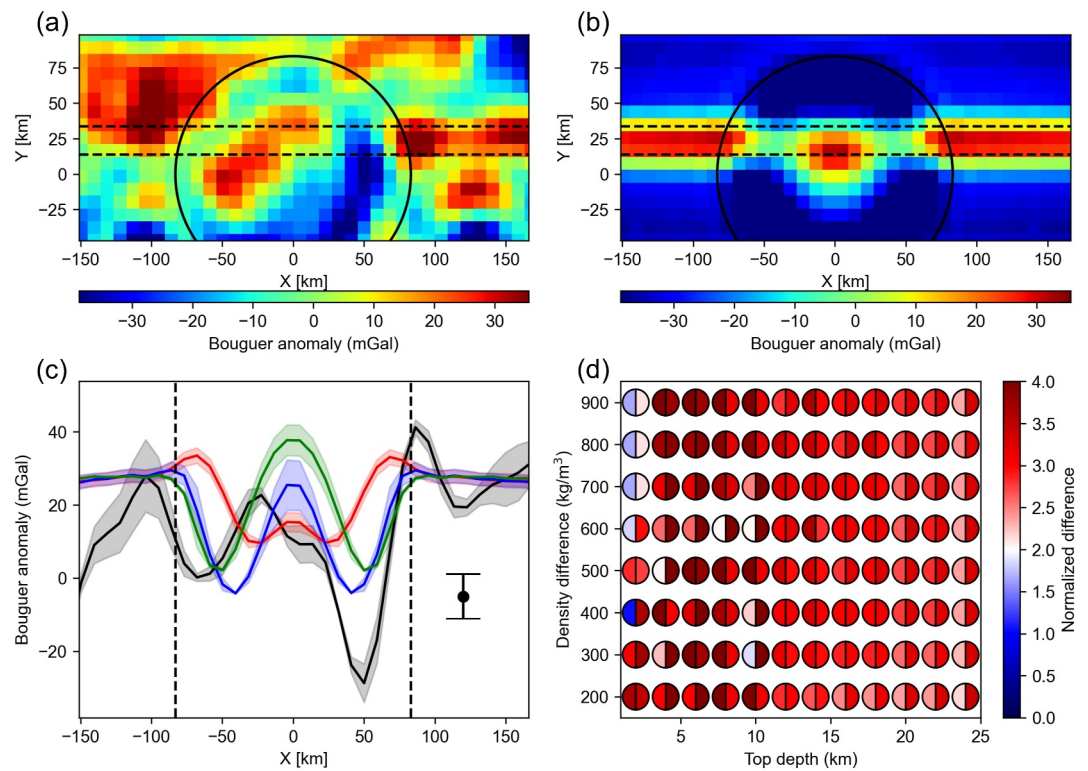


**Figure 7.** Comparison between simulations and the observed data. (a) The Bouguer anomaly map around Rowland crater. The solid black line shows the rim position. The area between the two black dashed lines is used for the comparison. Note that the coordinate is rotated to make the LGA direction parallel to the  $x$ -axis. (b) An example of a simulated Bouguer anomaly map when the density difference, top depth, and initial crustal porosity are assumed to be  $400 \text{ kg/m}^3$ ,  $10 \text{ km}$ , and  $2.5\%$ , respectively. (c) The averaged gravity profile within the compared area. The observed data is shown in the black line. The red, green, and blue lines show the gravity change by the LGA modification, porosity change, and the sum of these two effects. The shaded areas correspond to a standard deviation range within the compared area. The black error bar shows a standard deviation of the LGA gravity outside the crater. (d) The difference normalized by the standard deviation of LGA at the local maximum (left semi-circle) and minimum (right one) within the crater.

affected by both impact processes. Finally, the best-fit gravity model was determined for each set of assumed parameters.

#### 4.2. Rowland Crater on LGA1

Our numerical simulation suggests that the abrupt termination of LGA1 at Rowland's rim is not attributable to the crater formation. The simulated gravity profile exhibits a discrepancy from the gravity profile data inside the Rowland crater, particularly at the substantial gravity gap between the rim and center. The Bouguer anomalies within the area surrounded by the two black dashed lines in Figures 7a and 7b are averaged along the  $y$ -axis (the black, red, blue, and green lines in Figure 7c). The gravity anomaly and gradient data show that the gravity inside the Rowland crater drops for more than  $70 \text{ mGal}$  adjacent to the apparent LGA1 (Figure 7c) and appears terminated at the crater rim in the gravity gradient map (Figure 1b). This gravity drop is much larger than that caused by excavation and deformation in the crater formation. Figure 7b shows the case where the density difference, top depth, and initial crustal porosity are assumed to be  $400 \text{ kg/m}^3$ ,  $10 \text{ km}$ , and  $2.0\%$ , respectively. Figure 7c demonstrates that the gravity value after the collision decreases inside the crater. The simulated value exhibits a spatial pattern qualitatively similar to the observed data. The porosity reduction reproduces the positive gravity anomalies at the central part of the crater from the pre-impact state. However, the LGA-like gravity still appears to continue throughout the Rowland crater because the gravity drop near the rim is limited to approximately  $30 \text{ mGal}$  and less than half the observed drop (Figure 7b).

The discrepancy between the numerical simulation and the observed gravity anomalies is caused by the remaining root of the intrusion. To account for the high gravity at the central part of Rowland simultaneously, the best-fit



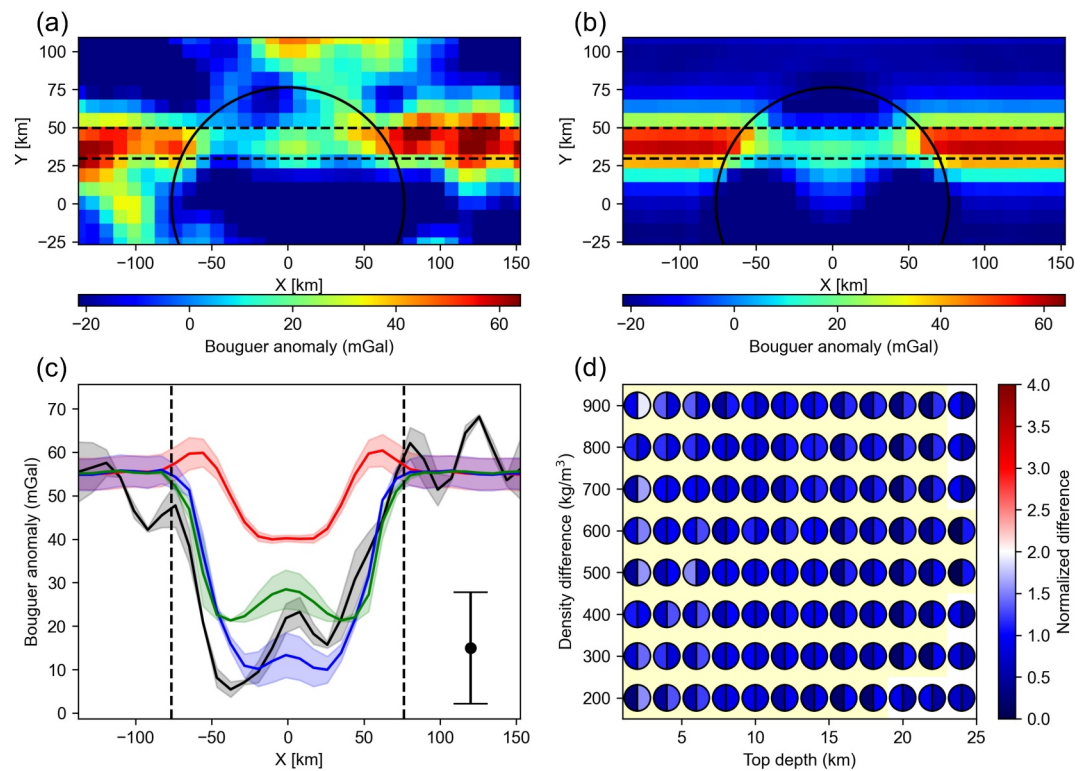


**Figure 8.** Comparison between the simulated and observed gravity anomalies at Roche crater. Panels (a–d) are drawn in the same manner as Figure 7. (b) The density difference, top depth, and initial crustal porosity are assumed to be the same as Figure 7b. (d) The color behind the circle is yellow when the necessary gravity decrease solely from the porosity change is less than 40 mGal.

dilatancy model makes the gravity drop of only 15 mGal near the rim, as shown by the green line in Figure 7c. In contrast, the LGA modification decreases the Bouguer gravity by only 15 mGal in the crater in this case. As demonstrated in Figure 6, the crater formation cannot destroy all the structures of the intrusion. Therefore, the root of the intrusion remains beneath the simulated crater, failing to explain the complete termination of LGA at Rowland's rim in the observed data (Figure 1b).

Any simulated gravity profiles cannot describe the specific gravity signature inside the Rowland crater, implying that LGA1 is not continuous under the Rowland crater. To make sure of this finding, we investigate all the sets of assumed density and top depth. The differences in the average gravity profiles between observation and simulation were calculated (black and blue lines in Figure 7c). While the difference appears large, we need to consider the extent of the LGA variation itself carefully. For this purpose, the difference is normalized by a standard deviation of LGA gravity outside the Rowland crater (black error bar in Figure 7c). To quantitatively examine the similarity between the gravity value and profile shape, we focus on the normalized difference at the local gravity minimum and maximum inside the crater. In Figure 7d, the normalized differences between the observation and simulation are shown for all the assumed parameter sets. Although the local maximum can be reproduced within two standard deviation ranges for a couple of parameter sets, the difference at the local minimum is always larger than three standard deviations. This implies that the great gravity gap next to the terminator of LGA cannot be attributed to the cratering excavation and/or pre-impact LGA variation, proving that LGA1 did not extend beyond the Rowland rim even before the crater formation.

### 4.3. Roche Crater on LGA2

Contrary to LGA1, our simulation successfully reproduces gravity signatures similar to the LGA2 values observed inside the Roche crater. As shown in Figures 1d and 8a, the gravity inside the Roche is weaker than that outside but a linear feature extends across the Roche crater. This feature is also seen in our numerical simulation. Figures 8b and 8c demonstrate an example case simulated under the same assumption of the density difference

and top depth as Figure 7. The excavation and deformation of LGA obscure the linear feature, but the remaining root of LGA beneath the excavation depth of Roche still appears to be a continuation of the LGA. The average gravity decrease of approximately 50 mGal within the Roche crater is less pronounced than that observed within the Rowland crater. As shown in Figure 8c, this moderate decrease can be attributed to the combined effect of the LGA modification and porosity production due to the Roche formation. This comparison between simulated and observed gravity implies that LGA2 was affected by the crater formation but not entirely destroyed.

The comparison between the simulation and data for all the parameter sets confirms the effect of the impact cratering on LGA2. The black line in Figure 8c shows that the averaged gravity within the Roche crater floor has a variation with a range of 20 mGal. Given the variation of the LGA2 gravity outside Roche crater, we investigate whether the simulated profile matches the data at the local maximum and minimum in the same way as LGA1. Figure 8c depicts that the gravity signature always agrees with the observation within 1.5 standard deviations. Thus, the porosity and intrusion modification explain the LGA2 gravity decrease inside the Roche crater.

Figure 8d also implies that the favorable top depth of the intrusion is shallower than 22 km. As Figure 8c demonstrates, the intrusion body at the deep area undergoes modification but remains in almost the same position. The gravity decrease by the LGA modification is hence less than 5 mGal if the whole intrusion exists deeper than 22 km before the impact. In addition, the gravity decrease is limited to the locations nearest to the crater center (Figure 8c), where the depth of the excavated and modified region is the deepest on LGA2. This value is too small to explain the observed gravity decrease of 50 mGal even with negative gravity from porosity production because the observed gravity decreases inside lunar craters with a size similar to the Roche range of less than 40 mGal (Soderblom et al., 2015). Thus, the observed gravity decrease is unlikely to be explained by the LGA intrusion with a top depth greater than 22 km.

## 5. Discussion on Each LGA History

### 5.1. LGA1

The spectral and gravitational features around LGA1 imply that Rowland crater did not excavate LGA1, possibly meaning that the intrusion of LGA1 postdates the Rowland crater. As demonstrated in our gravity simulations, the observed gravity profile with a substantial gravity drop does not match the assumption that the magmatic intrusion of LGA1 pre-existed beneath the area currently occupied by Rowland crater. This interpretation is also supported by the gravity anomaly perpendicular to the LGA direction (Text S2 in Supporting Information S1). These results allow us to propose four possible scenarios: that Rowland crater was formed coincidentally just next to the edge of LGA1; that LGA1 intrusion is composed of LCP-bearing magma; that non-axisymmetric processes occurred inside Rowland; or that LGA1 was formed after Rowland crater. Although the first hypothesis cannot be ruled out, the probability of such a “lucky” impact is low. The highland crater density (Head et al., 2010; Heyer et al., 2023) can be multiplied by the area where a crater may be located with its rim overlapping the terminators of all the 20 LGAs within the gravity resolution. This calculation yields an expectation of 0.17 for the number of craters that are 160 km or larger in diameter and located in contact with LGA terminators.

The second possibility is the LCP composition of the LGA1 material. The Apollo samples have revealed the presence of plutonic noritic rocks known as Mg-suite (e.g., Shearer et al., 2015). Considering the formation age of Mg-suite, which is estimated to be  $\sim 4.3$  Ga (e.g., Carlson et al., 2014; Nyquist & Shih, 1992; B. Zhang et al., 2021), Mg-suite has been thought to be formed via decompression of lower mantle material during the mantle overturn (e.g., Prissel et al., 2023; Shearer et al., 2015). Because the density of Mg-suite melt is lower than that of the mare basalt, Mg-suite melt is expected to intrude into the lunar crust and is possible to be detected on the gravity map (Prissel et al., 2016; Sori et al., 2016). If the LGA1 arises from a subsurface Mg-suite intrusion, the absence of HCP around Rowland could be explained.

The second possibility is quantified by the simulation of gravity anomalies under the presumption of an Mg-suite intrusion. Assuming the Mg-suite density for LGA, the aforementioned simulations with iSALE were repeated. Because of the low concentration of Fe, the melt of Mg-suite is lighter than that of typical mare basalt by 200–300 kg/m<sup>3</sup> depending on its parental composition (Prissel et al., 2016). Assuming that the solidified Mg-suite intrusion is as dense as noritic rocks in Apollo samples (Kiefer et al., 2012), its density is compared with the vertical density distribution within the farside-highland crust (Goossens et al., 2020; Figure S12a in Supporting Information S1). At a depth deeper than 20 km, the density of noritic rocks is almost the same as that of the

surrounding crust, meaning that intrusions below 20 km do not contribute to the positive LGA. Thus, the LGA structure parameter sets were prepared by fitting a rectangular intrusion with a bottom depth of 20 km. Then, the gravity profile after the impact was simulated in the same way as Section 4.1 and compared with the gravity within Rowland.

Our simulations demonstrate that the root of the Mg-suite intrusion remains after the impact even when the intrusion is confined at a depth shallower than 20 km. Thus, the Mg-suite hypothesis is unlikely. Because the excavation depth of the crater decreases with the distance from the crater center, a more intrusive body remains in the subsurface nearer the rim (Figure S12b in Supporting Information S1). As a result, the remaining root shallower than 20 km contributes to the residual anomaly within Rowland (Figure S12c in Supporting Information S1). This feature is seen for all the parameter sets (Figure S12d in Supporting Information S1) and hence is inconsistent with the observed LGA1. As discussed in Section 4, this result infers the formation of LGA1 later than Rowland at the Nectarian age. Considering that the age of Mg-suite formation is much older than the Rowland formation, this cross-cutting relationship does not agree with the hypothesis of Mg-suite intrusion at LGA1.

As the third possibility, non-axisymmetric processes inside Rowland might have contributed to the discrepancy between the observed data and models. Our axisymmetric simulation does not account for all geophysical/geological processes that may have occurred. For instance, the gravity field inside Rowland is not axisymmetric but has a semi-arcuate variation (Figure 7a). This asymmetry might be caused by an oblique impact of the Rowland formation; however, the difference in directions between LGA1 and the axis of the semi-arcuate gravity anomaly excludes the possibility of an enhanced excavation of subsurface material locally above LGA1. In addition, the semi-arcuate negative gravity anomaly within Rowland shows no rise above the LGA1-extended area (Figure S8 in Supporting Information S1). Alternatively, the formation of the Rowland-Y crater (Figure 1a) might have affected the post-impact gravity field, but its influence is insufficient to explain the abrupt termination. According to the lunar crater analysis by Soderblom et al. (2015), the gravity depression caused by a 50-km-sized crater is less than 10 mGal on average. Furthermore, it is noteworthy that these asymmetric processes could have influenced the Roche case as well, while our simulation does not require any asymmetry to reproduce the LGA2 profile inside Roche.

The fourth possibility is that the LGA1 magma began to intrude into the crust after the crater formation but terminated at the rim of the Rowland crater. While all the unmodeled possibilities are not completely excluded, this scenario offers a straightforward interpretation of the lack of gravity signature rather than the other hypotheses considered above. The termination of LGA1 may be attributed to Rowland's topography. The orientation of dike intrusion is dependent on the stress state of the intruded media. It follows the direction perpendicular to the maximum tensile stress at the time of its formation (e.g., Watanabe et al., 2002). In particular, a crater-like round depression generates a stress field in which the crack-opening direction favors a concentric orientation. As the demonstration of a magma ascent beneath lunar floor-fractured craters by Michaut et al. (2020), unloading by a crater bends the trajectory of dikes beneath the crater, and magma ascends toward the rim of the above crater. In Figure 1, a negative gravity gradient of LGA1 does not extend into the Rowland crater but rather curves along the rim from the terminated point. Similar ring dike structures are evident around other impact basins such as Orientale (Andrews-Hanna et al., 2018). A ring fault made by a giant basin formation is regarded as a conduit for magma ascent. Although the size of the Rowland crater is smaller than craters accompanied by such a tectonic fault, the paleo stress field caused by Rowland's unloading could potentially bend the direction of magma intrusion around the rim of Rowland, resulting in an abrupt termination of the LGA1 gravity signal.

The above discussion on the LGA1 formation scenario may delay the LGA1 formation age and prolong the ancient lunar expansion. Previous studies have argued that the age of LGA1 is older than the Nectarian age in various ways. Sawada et al. (2016) estimated by crater-counting that the surface age around LGA1 is  $4.20^{+0.02}_{-0.03}$  Ga, corresponding to pre-Nectarian age. However, their argument does not agree with the cross-cutting relationship found by our analysis, perhaps indicating that the surface age on LGA1 does not represent the timing of subsurface intrusion. In addition, Liang and Andrews-Hanna (2022) argue that LGA1 is likely to predate the Rowland formation. They attribute the apparently abrupt termination of LGA1 at Rowland's rim to a reduction in the density contrast between the crust and LGA1 intrusion by the crater-forming shock waves, but their hypothesis is inconsistent with our numerical results that incorporate the porosity change. On the other hand, they also point out that the LGA1 gravity remains but becomes a little ambiguous beneath the Upper-Imbrium-aged Schjellerup



crater. This feature is similar to our numerical simulations of crater obliteration on LGA2. Therefore, the LGA1 formation started after the Nectarian age and probably ended by the Upper-Imbrium age. This is the youngest age estimation of LGAs on the Moon at present. From the apparent cross-cutting relationships of LGAs with two giant basins, the Crisium and South-Pole-Aitken basins, Andrews-Hanna et al. (2013) constrain that the LGAs were formed within the pre-Nectarian to early Nectarian time frame. Our geological analysis implies that the lunar expansion accompanied by the LGA formations perhaps continued beyond the Nectarian age as predicted by various thermal models of the Moon (U et al., 2022; N. Zhang et al., 2013a, 2013b). This new estimation range of the lunar expansion stage does not contradict previous estimates of the transition into the global contraction regime around 2.8 Ga (Ono et al., 2009).

## 5.2. LGA2

Our gravity simulation constrains the LGA2 formation age and is consistent with our discovery of HCP exposures in the periphery. Although a decisive conclusion is difficult to reach, consistency between our gravity simulations and the observed Bouguer anomalies reasonably implies the intrusion formation before cratering. This finding indicates that the Roche-forming impact postdates the magmatic intrusion of LGA2. Roche is a Nectarian-aged crater (Wilhelms & El-Baz, 1977), and the absolute age of a light plain within it is estimated to be 3.91 Ga from the crater size-frequency distribution (Hiesinger et al., 2013). Therefore, given that LGA2 postdates the South-Pole-Aitken basin formation (Andrews-Hanna et al., 2013), our analysis implies that the LGA2 formation occurred within the pre-Nectarian to Nectarian age. This cross-cutting relationship is also consistent with the hypothesis that the discovery of HCP exposures may have originated from an ancient magma intrusion excavated by Roche crater. Thus, the ejecta from the Roche crater could contain a certain portion of LGA material. In fact, most of the HCP exposures discovered in our spectral analysis are located within the continuous ejecta region (Melosh, 1989; Moore et al., 1974).

On the other hand, the majority of non-mare HCP exposures that we found are not located within the area predicted in our axisymmetric simulations. The RGB-composite and FeO maps show that the basaltic materials are identified in the northern area of Roche crater (Figure S2 in Supporting Information S1). However, the LGA materials traced in our simulation are deposited mainly in the northern-eastern area. Figure 9 shows the distribution of LGA materials expected to deposit on the surface in our simulation. In light of the spectral dominance of LCP of highland regolith at craters smaller than 10 km in diameter, the thickness of the top-surface mixing layer is estimated to be a minimum of 1 km (Yamamoto et al., 2015). Therefore, the LGA material whose final depth from the surface is 1 km or deeper is traced in this analysis (three red lines in Figure 9). The distribution depends on the assumed density and top depth. For example, if the density is high, the width of the intrusion becomes narrow to satisfy the mass conservation required from the observed gravity anomaly. Then, the portion of intrusions close to the crater center decreases. Because the excavation depth decreases with the distance from the center, the volume of the excavated LGA source is reduced (yellow area in Figure 9). The top depth of the intrusion is also a significant factor, as a shallower intrusion is more susceptible to excavation (yellow lines in Figure 9). Therefore, when the shallowest top depth and lowest density are assumed, the simulated ejecta distribution is the broadest and covers some HCP exposures discovered around the Roche's rim and at the wall of Roche-B crater. We tested all the assumed parameter sets; however, the predicted coverage of LGA-containing ejecta did not contain all the discovered HCP exposures (white crosses in Figure 9).

One possible explanation for the discrepancy between the ejecta distribution and the majority of HCP exposure positions is the oblique impact of the Roche formation. Figure S11 in Supporting Information S1 shows the topography (SLDEM2015) around Roche crater and the highest rim positions. The topography data were divided into 1-degree azimuth bins, assuming the crater center to be 42.37°S and 136.54°E, and the highest position in each bin was extracted. To prevent potential contamination by ejecta from the Pauli crater, the positions within its continuous ejecta region were conservatively eliminated from this analysis. After fitting an ellipse to the extracted points, we found that the Roche crater is elongated almost along the N-S direction with a semi-minor axis smaller than a semi-major axis by 7%. According to the scaling relationships proposed by (Davison & Collins, 2022), this diameter ratio corresponds to a crater formation with an impact angle of 45–50°. Despite such a moderate impact angle, the ejecta blanket displays an asymmetry, with a concentration in the impact direction (e.g., Shuvalov, 2011). Thus, the HCP discoveries centered in the northern area of Roche crater are perhaps attributed to a Roche-forming impact from the southern direction.

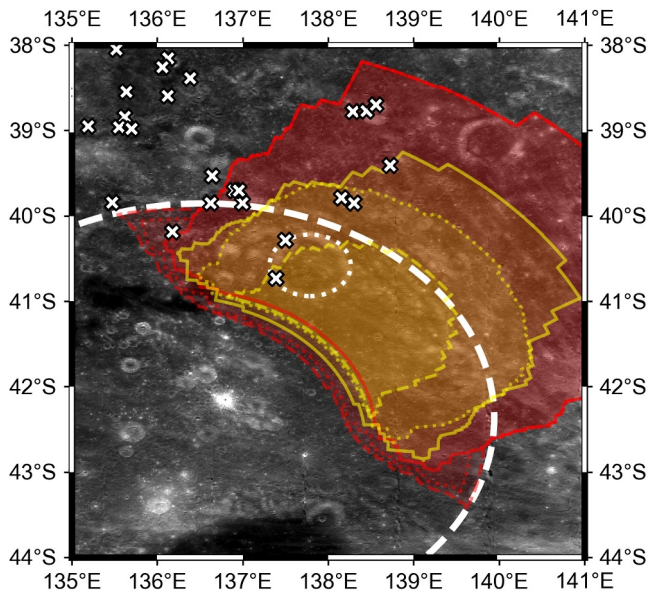


**Figure 9.** The deposition distribution of the LGA-containing ejecta around Roche crater. The white dashed and dotted lines show the rims of Roche and Roche B craters, respectively. The non-white lines show distributions of ejected LGA material for different sets of the assumed density and top depth. The red area shows the case for the density difference and top depth of  $200 \text{ kg/m}^3$ , 2 km, respectively. The red solid, dotted, and dashed lines show the area where the LGA tracers finally deposited at a depth shallower than 1, 2, and 3 km are considered. The yellow area shows the case for the density difference of  $400 \text{ kg/m}^3$ . The yellow solid, dotted, and dashed lines correspond to the assumed top depths of 2, 6, and 10 km, respectively. The white crosses are the locations of the discovered high-calcium pyroxenes exposures, respectively.

Another basaltic source of these HCP exposures, particularly in the case of the peripheries of newly identified mare patches (Figure S3 in Supporting Information S1), could be shallow subsurface magmatic intrusions whose spatial scale is too small to be resolved as LGAs. From  $M^3$  spectroscopy, Corley et al. (2018) have detected some olivine exposures around LGA2. However, these detections are not present at the exact location of the LGA, implying that other shallow and small magmatic intrusions are exposed by impacts. Since an ascending magma is predicted to be stalled and cooled before the eruption due to the thick crust in the lunar farside (Head & Wilson, 2017; Taguchi et al., 2017; Wilson & Head, 2017), the periphery of Roche crater is possibly a site of the stalled magma as well. In particular, the northern region of Roche crater has some small mare patches in the low topography (Figure S5 in Supporting Information S1) and might have experienced volcanic activity in the past. Although the ejecta from the present maria is not the source of these exposures, HCP from these small subsurface intrusions might be contained in the regolith of this region due to the later impact mixing and possibly exposed at the discovered points. Note that the cryptomare material is not likely the source of the HCP exposures since no dark-halo craters have been identified around the Roche crater (Izquierdo et al., 2024; Whitten & Head, 2015a). Regardless of whether the source of HCP exposures is the LGA body or the small subsurface intrusions, the composition of analyzed exposures should reflect that of the ancient magma and provide insights into the compositions of ancient subsurface intrusions.

### 5.3. LGA20

In contrast with LGA1 and 2, the faint gravity signal of LGA20 precludes a quantitative investigation into the exposure candidates around Edison crater. The Bouguer gradient map shows an ambiguous continuation of LGA20 into the Edison crater (Figure 1f). The Bouguer anomaly value inside the crater is 20 mGal less than that outside it. Although this small gravity drop can be

attributed solely to porosity variation induced by the crater formation, this feature is qualitatively similar to LGA2, suggesting the possibility of LGA material distribution in the periphery. Given the shallow excavation depth of Edison crater, a top depth shallower than 6 km is necessary for the ejection of the intrusive body. The floor of Edison crater and nearby Lomonosov crater is filled with lava after their formation, meaning that magma may have ascended to a depth of at least a few kilometers in this region. Thus, the LGA20 intrusion could have been stalled at a shallow subsurface and excavated by the Edison crater, resulting in the detection of the LGA material as HCP exposures.

Another possible source is a mixture of ancient mare material within the regolith around LGA20. Previous works have identified a cryptomare in the southeastern area of Edison. Geological categorization by Giguere et al. (2003) suggests that an ancient mare is covered by a light plain deposit in the Lomonosov-Fleming region. However, HCP exposures were also identified outside these cryptomare regions although Giguere et al. (2003) defined the locations of HCP exposures as pyroclastic deposits, which is inconsistent with our hyperspectral analysis. On the other hand, according to Whitten and Head (2015b) who surveyed cryptomaria all over the Moon, the area near Edison is included in the Lomonosov-Fleming cryptomare. In the central region of this cryptomare, an 8-km crater has an obvious dark halo of ancient basalt (Giguere et al., 2003). The floor of this crater has the same elevation level as that of the Edison crater. Therefore, if ancient basalt was distributed uniformly within this region before the Edison formation in the pre-Nectarian age, the ancient mare could be excavated and distributed as the HCP exposures. Nevertheless, the HCP exposures reflect the compositional information on magmatism during the lunar initial evolution as the age of the Lomonosov-Fleming cryptomare is estimated to be older than  $4.01^{+0.02}_{-0.03}$  Ga based on the superposed crater population (Whitten & Head, 2015b).

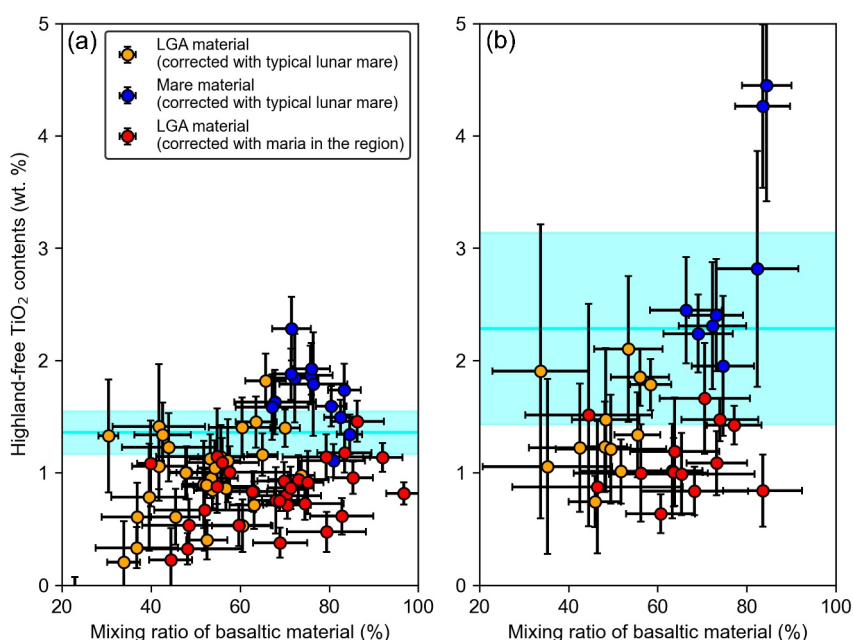


**Figure 10.** The inferred primordial  $\text{TiO}_2$  contents around (a) LGA2 and (b) LGA20. The  $x$ - and  $y$ -axis are the estimated mixing ratio of original basaltic material and highland-free  $\text{TiO}_2$  contents in wt. %. The orange and blue points are corrected values of exposures and maria under the assumption of a typical FeO content of lunar basalt. The red points are corrected values in the use of the average FeO contents of maria within the analyzed region. The cyan lines and shades are the average and standard deviation range of the mare values without corrections.

## 6. Implications to Ancient Lunar Magmatism

The aforementioned analysis and discussion suggest that the HCP exposures around LGA 2 and 20 contain ancient basaltic materials and possibly ejecta from the subsurface massive magmatic intrusions. Although our gravity simulation does not conclusively confirm the discovered HCP exposures as the subsurface LGA material, the consistency between the spectral and gravity analyses allows us to discuss the possible composition of magma directly related to the ancient lunar expansion. In particular, there are mare patches younger than the excavated material around both LGAs. Kato et al. (2017) showed that  $\text{TiO}_2$  contents vary with the age of the mare unit in the PKT region as a consequence of magma source transition. A comparison of titanium contents between the excavated ancient material and the nearby young maria would therefore allow us to interpret the compositional evolution of volcanism in the analyzed regions. However, the discovered HCP does not directly reflect the original composition since they are possibly contaminated by highland material, as seen in Figure 4.

To infer the primordial compositions of the HCP exposures, the highland contamination is corrected by estimating the mixing ratio from FeO contents. Assuming the FeO abundances of uncontaminated mare and highland material and the  $\text{TiO}_2$  abundance of highland material, both the highland-free  $\text{TiO}_2$  contents of excavated basaltic material and the mixing ratio of highland are estimated from the MI data analysis. The FeO and  $\text{TiO}_2$  contents of highland regolith are set at 4.0 and 0.3 wt. %, respectively, following Giguere et al. (2003). Two assumptions are made regarding the original FeO abundance of the HCP exposures: the average value of nearby maria or a typical value of lunar basalt of 18 wt. %. The first assumption may underestimate the  $\text{TiO}_2$  value because all the maria are contaminated by highland regolith to a certain extent. For example, the old mare inside Edison crater has an albedo higher than other maria (Figure 1), which indicates an ongoing transition from a highland-contaminated mare to a cryptomare (Giguere et al., 2003). On the other hand, the second value is higher than all the maria nearby LGAs (Figure 4) and thus gives us an upper limit of  $\text{TiO}_2$  contents. Therefore, the primordial LGA composition falls between these two estimations.

Figure 10 shows the inferred values of the mixing ratio of basaltic material and  $\text{TiO}_2$  content. It should be noted that the mare  $\text{TiO}_2$  estimation is also corrected under the second assumption of FeO abundance. Similarly to nearby younger maria, the corrected highland-free  $\text{TiO}_2$  contents of HCP exposures range from very-low- to low-

Ti basalt, indicating the possibility of the same magma source. Figure 10 depicts the mixing ratio of basaltic material and  $\text{TiO}_2$  estimated after removing highland contamination. With both the FeO assumptions, the primordial  $\text{TiO}_2$  contents are always lower than 2.5 wt. % at both LGA 2 and 20. The young mare basalts are mostly distributed from 1 to 3 wt. %. It is known that lunar samples from the Apollo and Luna missions show a bimodal distribution of  $\text{TiO}_2$  contents (Neal & Taylor, 1992). All the observed values at the HCP exposures and nearby maria are in the same lower class, which consists of very-low- (<1 wt. %) or low (1–6 wt. %)  $\text{TiO}_2$  basalt.

The similarity of  $\text{TiO}_2$  contents between LGA2 and 20 in Figure 10 perhaps shows a universal generation of low-titanium magma from the IBC-poor upper mantle during the lunar expansion stage. Although our analyses may elucidate only the local composition of the lunar upper mantle, the mare above other LGAs supports the hypothesis that LGAs may be composed of low-titanium magma in general. For example, mare Marginis located on the eastern side of LGA4 is covered by low-titanium basalt (Panwar et al., 2023). In addition, LGA 11 and 12 have been identified around the mare Australe, which is composed of low-titanium basalt (Kato et al., 2017). Because melt as rich in titanium as lunar black glass is positively buoyant at depths shallower than 600–700 km (Xu et al., 2022), the IBC-rich melt can ascend toward the surface as a magma source, consequently increasing the titanium content in the basalt of the subsurface intrusions. This presumption contradicts the low-titanium content of LGA2 and 20 and suggests an IBC-poor upper mantle, at least in these two regions. Such a magma source lacking IBC has also been assessed for other regions based on 2.03-Ga basalt samples brought by the Chang'E-5 mission (Li et al., 2021; Tian et al., 2021). Although there is a debate on the titanium contents of the picked basalt clasts due to their tiny size, the samples are classified as low-Ti basalts by tracking the crystallization sequence from titanium in olivine (D. Zhang et al., 2022; N. Zhang et al., 2022). It should be noted that the LGA composition inferred from this study does not agree with the recent argument by Liang et al. (2024) that the polygonal pattern of LGAs surrounding the PKT region is a vestige of IBC residual after the mantle overturn. Because the PKT-surrounding LGAs have features at longer spatial wavelengths than farside ones (Liang & Andrews-Hanna, 2022), the formation mechanism and composition may not be comparable directly among LGAs in the PKT region and elsewhere.

In addition, the temporally identical categorization of titanium contents indicates a similar or perhaps common magma source for the LGA material (red and orange points in Figure 10) and nearby young maria (blue points in Figure 10). If the magma sources for the LGA intrusion and nearby young maria are common, the slight variation in titanium abundance implies that the magma source was compositionally uniform over a long period. The ages of the mare patches are younger than the crater we expect to excavate the LGA materials. At LGA 2, the maria inside Roche crater has a surface age of 1.70–2.25 Ga. The absolute age of the small maria between Roche and Eötvös also ranges from 1.93 to 3.06 Ga (Pasckert et al., 2015). These mare units are younger than Roche crater, which has a light plain with an age of 3.91 Ga (Hiesinger et al., 2013). The maria around LGA 20 have been classified as units of Imbrian age (Wilhelms & El-Baz, 1977) and are much younger than the pre-Nectarian-aged Edison crater. Thus, the similarity of the titanium contents between the maria and exposures implies that the composition of magma sources around these LGAs was almost uniform for 1 billion years or longer. Only a slight variation of less than 1 wt. % perhaps exists but is less than the 2–3 wt. % increase in  $\text{TiO}_2$  observed at the PKT region around 2.3 Ga (Kato et al., 2017).

This uniform composition around LGAs suggests a lack of IBC within the upper mantle in these regions from the ancient expansion phase to around 2 Ga. IBCs are thought to be laid over the core-mantle boundary and/or trapped within the mantle following the lunar mantle overturn (Hess & Parmentier, 1995; Zhao et al., 2019). These IBC materials are possibly accompanied by heat-producing elements. Because the solidus of IBCs is lower than that of the mantle-like olivine-orthopyroxene (Delano, 1990), IBCs may become less dense than the surrounding mantle and rise as a plume (N. Zhang et al., 2013a). Several numerical models have suggested that lunar hot mantle plumes from the IBC layer may have occurred around 2 Ga (de Vries et al., 2010; Hess & Parmentier, 1995). This mechanism has been considered as a possible source of the high-titanium magma eruption around 2 Ga, so-called Phase-2 volcanism, particularly in the PKT region (Hiesinger et al., 2003; Kato et al., 2017; Morota et al., 2011). However, the  $\text{TiO}_2$  variation between the LGA magma and young maria lies within 1 wt.% and is much less than that of the PKT region. This indicates that such a titanium-rich plume neither provides the young magma directly nor contaminates the magma source significantly in this farside region. Such a titanium-poor mantle in the farside could reflect the lunar dichotomy of IBC distribution. As seen in the  $\text{Mg}\#$  ( $\text{Mg}/(\text{Mg} + \text{Fe})$  in mole %) distribution (Ohtake et al., 2012), the farside crust crystallized from less-evolved magma and could lie over less IBC than the nearside crust. In addition, several numerical models have predicted that convection during the mantle overturn



results in the accumulation of IBC material less in the farside mantle than in the nearside one (Parmentier et al., 2002; D. Zhang et al., 2022; N. Zhang et al., 2022).

## 7. Conclusions

To estimate the composition of magmatism during the ancient lunar expansion, we investigated spectral and gravity data sets around three craters located on LGAs: Rowland crater on LGA1, Roche crater on LGA2, and Edison crater on LGA20. Although LGAs have no prominent spectral feature immediately above them, LGAs reduced inside these craters suggest that ancient magma could have been excavated and distributed around them. We first analyzed spectral absorption with the MI data from Kaguya and M<sup>3</sup> data from Chandrayaan-1 to characterize the ejecta from subsurface intrusion. Using an RGB-composite map with the absorption depths of 950, 1,050, and 1,250 nm, we surveyed non-mare basaltic exposures. The type of pyroxene at the discovered exposures was then examined with the MGM spectral deconvolution method. We next compared the gravity data with gravity simulated with iSALE to discuss whether the discovered exposures originated from the LGA intrusion. After the preparation of intrusion shape sets by fitting the gravity profile outside the crater, we numerically traced the subsurface modification, excavation, and porosity change to simulate how the pre-existing LGA is reduced by the impact.

In the case of Rowland, both the spectral and gravity analyses revealed that the LGA intrusion may not have been excavated by the cratering. No exposures exhibiting a clear indication of high-calcium pyroxene have been identified in the vicinity of Rowland crater. The simulated gravity does not match the observed gravity because the gravity signature of the intrusion cannot be destroyed due to the remaining root of the LGA intrusion even after the impact. Thus, the abrupt termination of LGA at the rim of Rowland cannot be attributed to Rowland's excavation. The formation probability of a crater in contact with the LGA terminator is low, and the possibility of LCP-composing LGA does not match the gravity simulation. While the possibility of a cross-cutting relationship with Rowland remains open, LGA1 formation may postdate the Rowland-forming impact, perhaps indicating that the lunar expansion stage may have lasted even after the Nectarian age.

In contrast, both Roche and Edison craters allow us to estimate the magma composition during the lunar expansion. In their peripheries, more than 40 candidates of basaltic exposures are identified, the majority of which are accompanied by high-calcium pyroxene. Because the contribution of exogenic contamination, such as ejecta from the mare region, is not likely dominant, these exposures are hypothesized to originate from the subsurface LGA intrusion. The gravity simulation with iSALE also supports this hypothesis. Although the size of the Edison crater is insufficient for quantitative comparison, a gravity drop similar to LGA2 inside Roche is reproduced in our modeling. In addition, some exposures are located inside the ejecta blanket containing the LGA2 material. After correcting contamination by highland regolith using the FeO contents, the LGA intrusion is estimated to be composed of low-titanium magma. In particular, small young maria around LGA2 with ages of 2–3 Ga also consist of low-titanium basalt. This similarity might imply that the magma source region in the upper mantle lacks the IBC material and is compositionally uniform over a long period.

This study demonstrates that integrating gravity data with cratering simulations can provide a novel approach to investigating the chronology of the planetary interior structure based on its cross-cutting relationship with superposing craters. As the crater formation cannot erase all the pre-existing gravity signatures, subsurface modification simulations can be used to infer the ages of structures within the crust, such as giant dikes. When combined with high-resolution spectral data, it is also possible to assess the composition of subsurface density anomalies. This multi-faceted analysis of spectral and geodetic data sets will enhance our understanding of the ancient thermal history of other planets, particularly when high-resolution gravity anomaly data are acquired by GRAIL-like exploration missions in the future.

## Data Availability Statement

All the MI data sets can be downloaded via the SELENE data archive system in the Data ARchives and Transmission System (DARTS) of JAXA (<https://darts.isas.jaxa.jp/app/pdap/selene/>). The M3 data sets are stored in the PDS Imaging Node (<https://pds-imaging.jpl.nasa.gov/data/m3/>). All the topography and gravity data (SLDEM2015 and GRGM1200A\_BOUGUER) can be downloaded via the PDS Geoscience Node (<https://pds->

geosciences.wustl.edu). At present, the iSALE shock physics hydrocode is not fully open source, but an application for the use of iSALE may be made through <https://isale-code.github.io>.

### Acknowledgments

This work was supported by the IGPEES WINGS Program of the University of Tokyo, JSPS KAKENHI Grants JP22J12387, JP22K21344, JSPS Overseas Challenge Program for Young Researchers, and JSPS Overseas Research Fellowship, and the Publication Committee of National Astronomical Observatory of Japan. We gratefully acknowledge the developers of iSALE-2D (<https://isale-code.github.io>), including Kai Wünnemann, Dirk Elbeshausen, Boris Ivanov, and Jay Melosh. We used pySALEplot to analyze the output file of iSALE and thank Tom Davison for the development of pySALEplot. We appreciate Tabb Prissel and two anonymous reviewers for their valuable comments and suggestions, which helped us to improve the quality of the manuscript. We are also grateful to Hauke Hussmann, Alexander Stark, Mark Wieczorek, Takahiro Hiroi, and Kosuke Kurosawa for fruitful discussions and helpful comments. Numerical computations and analyses were carried out on the general-purpose PC cluster and the analysis servers at the Center for Computational Astrophysics, National Astronomical Observatory of Japan, respectively. Open Access funding enabled and organized by Projekt DEAL.

### References

- Amsden, A. A., Ruppel, H. M., & Hirt, C. W. (1980). SALE: A Simplified ALE computer program for fluid flow at all speeds. *Los Alamos National Laboratories Report*, LA-8095, (p. 101). Retrieved from [http://www.iaea.org/inis/collection/NCLCollectionStore/\\_Public/11/571/11571883.pdf?origin=publication\\_detail](http://www.iaea.org/inis/collection/NCLCollectionStore/_Public/11/571/11571883.pdf?origin=publication_detail)
- Andrews-Hanna, J. C., Asmar, S. W., Head, J. W., Kiefer, W. S., Konopliv, A. S., Lemoine, F. G., et al. (2013). Ancient igneous intrusions and early expansion of the moon revealed by GRAIL gravity gradiometry. *Science*, 339(6120), 675–678. <https://doi.org/10.1126/science.1231753>
- Andrews-Hanna, J. C., Head, J. W., Johnson, B. C., Keane, J. T., Kiefer, W. S., McGovern, P. J., et al. (2018). Ring faults and ring dikes around the Orientale basin on the Moon. *Icarus*, 310, 1–20. <https://doi.org/10.1016/j.icarus.2017.12.012>
- Barker, M. K., Mazarico, E., Neumann, G. A., Zuber, M. T., Haruyama, J., & Smith, D. E. (2016). A new lunar digital elevation model from the Lunar Orbiter Laser Altimeter and SELENE Terrain Camera. *Icarus*, 273, 346–355. <https://doi.org/10.1016/j.icarus.2015.07.039>
- Besse, S., Sunshine, J., Staid, M., Boardman, J., Pieters, C., Guasqui, P., et al. (2013). A visible and near-infrared photometric correction for Moon Mineralogy Mapper (M<sup>3</sup>). *Icarus*, 222(1), 229–242. <https://doi.org/10.1016/j.icarus.2012.10.036>
- Besse, S., Sunshine, J. M., & Gaddis, L. R. (2014). Volcanic glass signatures in spectroscopic survey of newly proposed lunar pyroclastic deposits. *Journal of Geophysical Research: Planets*, 119(2), 355–372. <https://doi.org/10.1002/2013JE004537>
- Boardman, J. W., Pieters, C. M., Green, R. O., Lundeen, S. R., Varanasi, P., Nettles, J., et al. (2011). Measuring moonlight: An overview of the spatial properties, lunar coverage, selenolocation, and related Level 1B products of the Moon Mineralogy Mapper. *Journal of Geophysical Research*, 116(6), E00G14. <https://doi.org/10.1029/2010JE003730>
- Botke, W. F., Vokrouhlický, D., Minton, D., Nesvorný, D., Morbidelli, A., Brassier, R., et al. (2012). An Archaean heavy bombardment from a destabilized extension of the asteroid belt. *Nature*, 485(7396), 78–81. <https://doi.org/10.1038/nature10967>
- Carlson, R. W., Borg, L. E., Gaffney, A. M., & Boyet, M. (2014). Rb-Sr, Sm-Nd and Lu-Hf isotope systematics of the lunar Mg-suite: The age of the lunar crust and its relation to the time of Moon formation. *Philosophical Transactions of the Royal Society A: Mathematical, Physical and Engineering Sciences*, 372(2024), 20130246. <https://doi.org/10.1098/rsta.2013.0246>
- Clark, R. N., Pieters, C. M., Green, R. O., Boardman, J. W., & Petro, N. E. (2011). Thermal removal from near-infrared imaging spectroscopy data of the Moon. *Journal of Geophysical Research*, 116(6), E00G16. <https://doi.org/10.1029/2010JE003751>
- Cloutis, E. A., & Gaffey, M. J. (1991). Pyroxene spectroscopy revisited: Spectral-compositional correlations and relationship to geothermometry. *Journal of Geophysical Research*, 96(E5), 22809–22826. <https://doi.org/10.1029/91je02512>
- Collins, G. S. (2014). Numerical simulations of impact crater formation with dilatancy. *Journal of Geophysical Research: Planets*, 119(12), 2600–2619. <https://doi.org/10.1002/2014JE004708>
- Collins, G. S., Melosh, H. J., & Ivanov, B. A. (2004). Modeling damage and deformation in impact simulations. *Meteoritics and Planetary Science*, 39(2), 217–231. <https://doi.org/10.1111/j.1945-5100.2004.tb00337.x>
- Collins, G. S., Melosh, H. J., & Wünnemann, K. (2011). Improvements to the  $\epsilon$ - $\alpha$  Porous compaction model for simulating impacts into high-porosity solar system objects. *International Journal of Impact Engineering*, 38(6), 434–439. <https://doi.org/10.1016/j.ijimpeng.2010.10.013>
- Corley, L. M., McGovern, P. J., Kramer, G. Y., Lemelin, M., Trang, D., Gillis-Davis, J. J., et al. (2018). Olivine-bearing lithologies on the Moon: Constraints on origins and transport mechanisms from M<sup>3</sup> spectroscopy, radiative transfer modeling, and GRAIL crustal thickness. *Icarus*, 300, 287–304. <https://doi.org/10.1016/j.icarus.2017.09.012>
- Dasgupta, R., Hirschmann, M. M., & Smith, N. D. (2007). Partial melting experiments of peridotite + CO<sub>2</sub> at 3 GPa and genesis of alkalic ocean island basalts. *Journal of Petrology*, 48(11), 2093–2124. <https://doi.org/10.1093/ptrology/egm053>
- Davison, T. M., & Collins, G. S. (2022). Complex crater formation by oblique impacts on the Earth and Moon. *Geophysical Research Letters*, 49(21), e2022GL101117. <https://doi.org/10.1029/2022gl101117>
- Delano, J. W. (1990). Buoyancy-driven melt segregation in the Earth's Moon. I. Numerical results. In *Lunar and Planetary Science Conference, 20th, Houston, TX, March 13–17, 1989, Proceedings (A90-33456 14-91)* (Vol. 4, pp. 3–12). Lunar and Planetary Institute.
- Denevi, B. W., Lucey, P. G., Hochberg, E. J., & Stutel, D. (2007). Near-infrared optical constants of pyroxene as a function of iron and calcium content. *Journal of Geophysical Research*, 112(E5), E05009. <https://doi.org/10.1029/2006JE002802>
- de Vries, J., van den Berg, A., & van Westrenen, W. (2010). Formation and evolution of a lunar core from ilmenite-rich magma ocean cumulates. *Earth and Planetary Science Letters*, 292(1–2), 139–147. <https://doi.org/10.1016/j.epsl.2010.01.029>
- Elkins-Tanton, L. T., Burgess, S., & Yin, Q. Z. (2011). The lunar magma ocean: Reconciling the solidification process with lunar petrology and geochronology. *Earth and Planetary Science Letters*, 304(3–4), 326–336. <https://doi.org/10.1016/j.epsl.2011.02.004>
- Giguere, T. A., Hawke, B. R., Blewett, D. T., Bussey, D. B. J., Lucey, P. G., Smith, G. A., et al. (2003). Remote sensing studies of the Lomonosov-Fleming region of the Moon. *Journal of Geophysical Research*, 108(11), 5118. <https://doi.org/10.1029/2003je002069>
- Goossens, S., Sabaka, T. J., Wieczorek, M. A., Neumann, G. A., Mazarico, E., Lemoine, F. G., et al. (2020). High-resolution gravity field models from GRAIL data and implications for models of the density structure of the Moon's crust. *Journal of Geophysical Research: Planets*, 125(2), 1–31. <https://doi.org/10.1029/2019JE006086>
- Green, R. O., Pieters, C., Mouroulis, P., Eastwood, M., Boardman, J., Glavich, T., et al. (2011). The Moon Mineralogy Mapper (M<sup>3</sup>) imaging spectrometer for lunar science: Instrument description, calibration, on-orbit measurements, science data calibration and on-orbit validation. *Journal of Geophysical Research*, 116(10), 1–31. <https://doi.org/10.1029/2011JE003797>
- Head, J. W., Fassett, C. I., Kadish, S. J., Smith, D. E., Zuber, M. T., Neumann, G. A., & Mazarico, E. (2010). Global distribution of large lunar craters: Implications for resurfacing and impactor populations. *Science*, 329(5998), 1504–1507. <https://doi.org/10.1126/science.1195050>
- Head, J. W., & Wilson, L. (2017). Generation, ascent and eruption of magma on the Moon: New insights into source depths, magma supply, intrusions and effusive/explosive eruptions (Part 2: Predicted emplacement processes and observations). *Icarus*, 283, 176–223. <https://doi.org/10.1016/j.icarus.2016.05.031>
- Hess, P. C., & Parmentier, E. M. (1995). A model for the thermal and chemical evolution of the Moon's interior: Implications for the onset of mare volcanism. *Earth and Planetary Science Letters*, 134(3–4), 501–514. [https://doi.org/10.1016/0012-821X\(95\)00138-3](https://doi.org/10.1016/0012-821X(95)00138-3)
- Heyer, T., Iqbal, W., Oetting, A., Hiesinger, H., van der Bogert, C. H., & Schmedemann, N. (2023). A comparative analysis of global lunar crater catalogs using OpenCraterTool – An open source tool to determine and compare crater size-frequency measurements. *Planetary and Space Science*, 231, 105687. <https://doi.org/10.1016/j.pss.2023.105687>
- Hiesinger, H., Head, J. W., Wolf, U., Jaumann, R., & Neukum, G. (2003). Ages and stratigraphy of mare basalts in Oceanus Procellarum, Mare Nubium, mare Cognitum, and Mare Insularum. *Journal of Geophysical Research*, 108(7), 5065. <https://doi.org/10.1029/2002je001985>

- Hiesinger, H., van der Bogert, C. H., Thiessen, F., & Robinson, M. S. (2013). Absolute model ages of light plains in the southern lunar hemisphere. In *Lunar and Planetary Science Conference* (pp. 4–5).
- Huang, Y. H., Soderblom, J. M., Minton, D. A., Hirabayashi, M., & Melosh, H. J. (2022). Bombardment history of the Moon constrained by crustal porosity. *Nature Geoscience*, *15*(7), 531–535. <https://doi.org/10.1038/s41561-022-00969-4>
- Isaacson, P. J., Petro, N. E., Pieters, C. M., Besse, S., Boardman, J. W., Clark, R. N., et al. (2013). Development, importance, and effect of a ground truth correction for the Moon Mineralogy Mapper reflectance data set. *Journal of Geophysical Research: Planets*, *118*(3), 369–381. <https://doi.org/10.1002/jgre.20048>
- Isaacson, P. J., Pieters, C. M., Besse, S., Clark, R. N., Head, J. W., Klima, R. L., et al. (2011). Remote compositional analysis of lunar olivine-rich lithologies with Moon Mineralogy Mapper (M<sup>3</sup>) spectra. *Journal of Geophysical Research*, *116*(4), 1–17. <https://doi.org/10.1029/2010JE003731>
- Ivanov, B. A., Deniem, D., & Neukum, G. (1997). Implementation of dynamic strength models into 2D hydrocodes: Applications for atmospheric breakup and impact cratering. *International Journal of Impact Engineering*, *20*(1–5), 411–430. [https://doi.org/10.1016/s0734-743x\(97\)87511-2](https://doi.org/10.1016/s0734-743x(97)87511-2)
- Izquierdo, K., Sori, M. M., Checketts, B., Hampton, I., Johnson, B. C., & Soderblom, J. M. (2024). Global distribution and volume of cryptomare and visible Mare on the Moon from gravity and dark halo craters. *Journal of Geophysical Research: Planets*, *129*(2), e2023JE007867. <https://doi.org/10.1029/2023JE007867>
- Kato, S., Morota, T., Yamaguchi, Y., Watanabe, S. I., Otake, H., & Ohtake, M. (2017). Magma source transition of lunar mare volcanism at 2.3 Ga. *Meteoritics and Planetary Science*, *52*(9), 1899–1915. <https://doi.org/10.1111/maps.12896>
- Kiefer, W. S., MacKe, R. J., Britt, D. T., Irving, A. J., & Consolmagno, G. J. (2012). The density and porosity of lunar rocks. *Geophysical Research Letters*, *39*(7), L07201. <https://doi.org/10.1029/2012GL051319>
- Klima, R. L., Dyar, M. D., & Pieters, C. M. (2011). Near-infrared spectra of clinopyroxenes: Effects of calcium content and crystal structure. *Meteoritics and Planetary Science*, *46*(3), 379–395. <https://doi.org/10.1111/j.1945-5100.2010.01158.x>
- Klima, R. L., Pieters, C. M., & Dyar, M. D. (2007). Spectroscopy of synthetic Mg-Fe pyroxenes I: Spin-allowed and spin-forbidden crystal field bands in the visible and near-infrared. *Meteoritics and Planetary Science*, *42*(2), 235–253. <https://doi.org/10.1111/j.1945-5100.2007.tb00230.x>
- Kumaresan, P. R., & Saravanavel, J. (2022). Compositional mapping and spectral analysis of Sulpicius Gallus dark mantling deposits using lunar orbital data sets including Chandrayaan-1 Moon Mineralogy Mapper. *Journal of the Indian Society of Remote Sensing*, *50*(7), 1301–1319. <https://doi.org/10.1007/s12524-022-01529-4>
- Laneuville, M., Wiczorek, M. A., Breuer, D., & Tosi, N. (2013). Asymmetric thermal evolution of the Moon. *Journal of Geophysical Research: Planets*, *118*(7), 1435–1452. <https://doi.org/10.1002/jgre.20103>
- Lemoine, F. G., Goossens, S., Sabaka, T. J., Nicholas, J. B., Mazarico, E., Rowlands, D. D., et al. (2014). GRGM900C: A degree 900 lunar gravity model from GRAIL primary and extended mission data. *Geophysical Research Letters*, *41*(10), 3382–3389. <https://doi.org/10.1002/2014GL060027>
- Li, Q. L., Zhou, Q., Liu, Y., Xiao, Z., Lin, Y., Li, J. H., et al. (2021). Two-billion-year-old volcanism on the Moon from Chang'e-5 basalts. *Nature*, *600*(7887), 54–58. <https://doi.org/10.1038/s41586-021-04100-2>
- Liang, W., & Andrews-Hanna, J. C. (2022). Probing the source of ancient linear gravity anomalies on the Moon. *Icarus*, *380*, 114978. <https://doi.org/10.1016/j.icarus.2022.114978>
- Liang, W., Broquet, A., Andrews-Hanna, J. C., Zhang, N., Ding, M., & Evans, A. J. (2024). Vestiges of a lunar ilmenite layer following mantle overturn revealed by gravity data. *Nature Geoscience*, *17*(4), 361–366. <https://doi.org/10.1038/s41561-024-01408-2>
- Lucey, P. G., Blewett, D. T., & Jolliff, B. L. (2000). Lunar iron and titanium abundance algorithms based on final processing of Clementine ultraviolet-visible images. *Journal of Geophysical Research*, *105*(E8), 20297–20305. <https://doi.org/10.1029/1999JE001117>
- Lucey, P. G., Blewett, D. T., Taylor, G. J., & Hawke, B. R. (2000). Imaging of lunar surface maturity. *Journal of Geophysical Research*, *105*(E8), 20377–20386. <https://doi.org/10.1029/1999JE001110>
- Lucey, P. G., & Hawke, B. R. (1988). A remote mineralogical perspective on gabbroic units in the lunar highlands. In *In Proceedings of the 18th Lunar and Planetary Science Conference* (pp. 355–363).
- Lucey, P. G., Norman, J. A., Crites, S. T., Taylor, G. J., Hawke, B. R., Lemelin, M., & Melosh, H. J. (2014). A large spectral survey of small lunar craters: Implications for the composition of the lunar mantle. *American Mineralogist*, *99*(11–12), 2251–2257. <https://doi.org/10.2138/am-2014-4854>
- Lucey, P. G., Taylor, G. J., Hawke, B. R., & Spudis, P. D. (1998). FeO and TiO<sub>2</sub> concentrations in the South Pole-Aitken basin: Implications for mantle composition and basin formation. *Journal of Geophysical Research*, *103*(E2), 3701–3708. <https://doi.org/10.1029/97JE03146>
- Malaret, E. P. (2011). *CH1-ORB Moon M3 4 L2 Reflectance Near-IR Spectral IMGS V1.0 PDS3 ID CH1-ORB-L-M3-4-L2-ReflectanceE-V1.0*. NASA Planetary Data System.
- McGetchin, T. R., Settle, M., & Head, J. W. (1973). Radial thickness variation in impact crater ejecta: Implications for lunar basin deposits. *Earth and Planetary Science Letters*, *20*(2), 226–236. [https://doi.org/10.1016/0012-821x\(73\)90162-3](https://doi.org/10.1016/0012-821x(73)90162-3)
- Melosh, H. J. (1989). *Impact cratering: A geologic process*. Oxford University Press; Clarendon Press. Retrieved from <http://www.loc.gov/catdir/enhancements/fy0638/88005353-t.html>
- Melosh, H. J., Freed, A. M., Johnson, B. C., Blair, D. M., Andrews-Hanna, J. C., Neumann, G. A., et al. (2013). The origin of lunar mascon basins. *Science*, *340*(6140), 1552–1555. <https://doi.org/10.1126/science.1235768>
- Melosh, H. J., Ryan, E. V., & Asphaug, E. (1992). Dynamic fragmentation in impacts: Hydrocode simulation of laboratory impacts. *Journal of Geophysical Research*, *97*(E9), 14735–14759. <https://doi.org/10.1029/92JE01632>
- Michaut, C., Pinel, V., & Maccaferri, F. (2020). Magma ascent at floor-fractured craters diagnoses the lithospheric stress state on the Moon. *Earth and Planetary Science Letters*, *530*, 115889. <https://doi.org/10.1016/j.epsl.2019.115889>
- Milbury, C., Johnson, B. C., Melosh, H. J., Collins, G. S., Blair, D. M., Soderblom, J. M., et al. (2015). Preimpact porosity controls the gravity signature of lunar craters. *Geophysical Research Letters*, *42*(22), 9711–9716. <https://doi.org/10.1002/2015GL066198>
- Miljković, K., Wiczorek, M. A., Collins, G. S., Solomon, S. C., Smith, D. E., & Zuber, M. T. (2015). Excavation of the lunar mantle by basin-forming events on the Moon. *Earth and Planetary Science Letters*, *409*, 243–251. <https://doi.org/10.1016/j.epsl.2014.10.041>
- Miljković, K., Wiczorek, M. A., Laneuville, M., Nemchin, A., Bland, P. A., & Zuber, M. T. (2021). Large impact cratering during lunar magma ocean solidification. *Nature Communications*, *12*(1), 1–18. <https://doi.org/10.1038/s41467-021-25818-7>
- Moore, H. J., Hodges, C. A., & Scott, D. H. (1974). Multiringed basins - Illustrated by Orientale and associated features. In *Proceedings of Lunar Science Conference 5th, Houston, Texas, March 18–22, 1974* (Vol. 1, pp. 71–100).
- Moriarty, D. P., & Pieters, C. M. (2018). The character of South Pole-Aitken Basin: Patterns of surface and subsurface composition. *Journal of Geophysical Research: Planets*, *123*(3), 729–747. <https://doi.org/10.1002/2017JE005364>

- Morota, T., Haruyama, J., Ohtake, M., Matsunaga, T., Honda, C., Yokota, Y., et al. (2011). Timing and characteristics of the latest mare eruption on the Moon. *Earth and Planetary Science Letters*, 302(3–4), 255–266. <https://doi.org/10.1016/j.epsl.2010.12.028>
- Neal, C. R., & Taylor, L. A. (1992). Petrogenesis of mare basalts: A record of lunar volcanism. *Geochimica et Cosmochimica Acta*, 56(6), 2177–2211. [https://doi.org/10.1016/0016-7037\(92\)90184-K](https://doi.org/10.1016/0016-7037(92)90184-K)
- Nyquist, L. E., & Shih, C. Y. (1992). The isotopic record of lunar volcanism. *Geochimica et Cosmochimica Acta*, 56(6), 2213–2234. [https://doi.org/10.1016/0016-7037\(92\)90185-L](https://doi.org/10.1016/0016-7037(92)90185-L)
- Ogawa, Y., Matsunaga, T., Nakamura, R., Saiki, K., Ohtake, M., Hiroi, T., et al. (2011). The widespread occurrence of high-calcium pyroxene in bright-ray craters on the Moon and implications for lunar-crust composition. *Geophysical Research Letters*, 38(17), L17202. <https://doi.org/10.1029/2011GL048569>
- Öhman, T. (2015). *LPI crater database*. Lunar & Planetary Institute.
- Ohtake, M., Haruyama, J., Matsunaga, T., Kodama, S., Morota, T., & Yokota, Y. (2008). Scientific objectives and specification of the SELENE Multiband Imager. *Advances in Space Research*, 42(2), 301–304. <https://doi.org/10.1016/j.asr.2007.04.041>
- Ohtake, M., Pieters, C. M., Isaacson, P., Besse, S., Yokota, Y., Matsunaga, T., et al. (2013). One Moon, Many Measurements 3: Spectral reflectance. *Icarus*, 226(1), 364–374. <https://doi.org/10.1016/j.icarus.2013.05.010>
- Ohtake, M., Takeda, H., Matsunaga, T., Yokota, Y., Haruyama, J., Morota, T., et al. (2012). Asymmetric crustal growth on the Moon indicated by primitive farside highland materials. *Nature Geoscience*, 5(6), 384–388. <https://doi.org/10.1038/ngeo1458>
- Ohtake, M., Uemoto, K., Yokota, Y., Morota, T., Yamamoto, S., Nakamura, R., et al. (2014). Geologic structure generated by large-impact basin formation observed at the South Pole-Aitken basin on the Moon. *Geophysical Research Letters*, 41(8), 2738–2745. <https://doi.org/10.1002/2014GL059478>
- Ono, T., Kumamoto, A., Nakagawa, H., Yamaguchi, Y., Oshigami, S., Yamaji, A., et al. (2009). Lunar radar sounder observations of subsurface layers under the nearside maria of the moon. *Science*, 323(5916), 909–912. <https://doi.org/10.1126/science.1165988>
- Osinski, G. R., Tornabene, L. L., & Grieve, R. A. F. (2011). Impact ejecta emplacement on terrestrial planets. *Earth and Planetary Science Letters*, 310(3–4), 167–181. <https://doi.org/10.1016/j.epsl.2011.08.012>
- Otake, H., Ohtake, M., & Hirata, N. (2012). Lunar iron and titanium abundance algorithms based on SELENE (Kaguya) multiband imager data. In *Texas: 43rd Lunar and Planetary Science Conference* (p. 1905).
- Panwar, N., Srivastava, N., Bhatt, M., & Bhardwaj, A. (2023). Compositional diversity in the Mare Marginis and Mare Smythii: An insight into the volcanism in the region. *Icarus*, 395, 115496. <https://doi.org/10.1016/j.icarus.2023.115496>
- Parmentier, E. M., Zhong, S., & Zuber, M. T. (2002). Gravitational differentiation due to initial chemical stratification: Origin of lunar asymmetry by the creep of dense KREEP? *Earth and Planetary Science Letters*, 201(3–4), 473–480. [https://doi.org/10.1016/S0012-821X\(02\)00726-4](https://doi.org/10.1016/S0012-821X(02)00726-4)
- Pasckert, J. H., Hiesinger, H., & van der Bogert, C. H. (2015). Small-scale lunar farside volcanism. *Icarus*, 257, 336–354. <https://doi.org/10.1016/j.icarus.2015.04.040>
- Pieters, C. M., Goswami, J. N., Clark, R. N., Annadurai, M., Boardman, J., Buratti, B., et al. (2009). Character and spatial distribution of OH/H<sub>2</sub>O on the surface of the moon seen by M3 on chandrayaan-1. *Science*, 326(5952), 568–572. <https://doi.org/10.1126/science.1178658>
- Piskorz, D., & Stevenson, D. J. (2014). The formation of pure anorthosite on the Moon. *Icarus*, 239, 238–243. <https://doi.org/10.1016/j.icarus.2014.06.015>
- Prissel, T. C., Whitten, J. L., Parman, S. W., & Head, J. W. (2016). On the potential for lunar highlands Mg-suite extrusive volcanism and implications concerning crustal evolution. *Icarus*, 277, 319–329. <https://doi.org/10.1016/j.icarus.2016.05.018>
- Prissel, T. C., Zhang, N., Jackson, C. R. M., & Li, H. (2023). Rapid transition from primary to secondary crust building on the Moon explained by mantle overturn. *Nature Communications*, 14(1), 5002. <https://doi.org/10.1038/s41467-023-40751-7>
- Robinson, M. S., Brylow, S. M., Tschimmel, M., Humm, D., Lawrence, S. J., Thomas, P. C., et al. (2010). Lunar reconnaissance orbiter camera (LROC) instrument overview. *Space Science Reviews*, 150(1–4), 81–124. <https://doi.org/10.1007/s11214-010-9634-2>
- Sato, H., Robinson, M. S., Lawrence, S. J., Denevi, B. W., Hapke, B., Jolliff, B. L., & Hiesinger, H. (2017). Lunar mare TiO<sub>2</sub> abundances estimated from UV/Vis reflectance. *Icarus*, 296, 216–238. <https://doi.org/10.1016/j.icarus.2017.06.013>
- Sawada, N., Morota, T., Kato, S., Ishihara, Y., & Hiramatsu, Y. (2016). Constraints on timing and magnitude of early global expansion of the Moon from topographic features in linear gravity anomaly areas. *Geophysical Research Letters*, 43(10), 4865–4870. <https://doi.org/10.1002/2016GL068966>
- Scholten, F., Oberst, J., Matz, K. D., Roatsch, T., Wählisch, M., Speyerer, E. J., & Robinson, M. S. (2012). GLD100: The near-global lunar 100 m raster DTM from LROC WAC stereo image data. *Journal of Geophysical Research*, 117(3), 1–12. <https://doi.org/10.1029/2011JE003926>
- Shearer, C. K., Elardo, S. M., Petro, N. E., Borg, L. E., & McCubbin, F. M. (2015). Origin of the lunar highlands Mg-suite: An integrated petrology, geochemistry, chronology, and remote sensing perspective. *American Mineralogist*, 100(1), 294–325. <https://doi.org/10.2138/am-2015-4817>
- Shuvalov, V. (2011). Ejecta deposition after oblique impacts: An influence of impact scale. *Meteoritics and Planetary Science*, 46(11), 1713–1718. <https://doi.org/10.1111/j.1945-5100.2011.01259.x>
- Snyder, G. A., Taylor, L. A., & Neal, C. R. (1992). A chemical model for generating the sources of mare basalts: Combined equilibrium and fractional crystallization of the lunar magmasphere. *Geochimica et Cosmochimica Acta*, 56(10), 3809–3823. [https://doi.org/10.1016/0016-7037\(92\)90172-F](https://doi.org/10.1016/0016-7037(92)90172-F)
- Soderblom, J. M., Evans, A. J., Johnson, B. C., Melosh, H. J., Miljkovic, K., Phillips, R. J., et al. (2015). The fractured Moon: Production and saturation of porosity in the lunar highlands from impact cratering. *Geophysical Research Letters*, 42(17), 6939–6944. <https://doi.org/10.1002/2015GL065022>
- Sori, M. M., Zuber, M. T., Head, J. W., & Kiefer, W. S. (2016). Gravitational search for cryptovolcanism on the Moon: Evidence for large volumes of early igneous activity. *Icarus*, 273, 284–295. <https://doi.org/10.1016/j.icarus.2016.02.009>
- Speyerer, E. J., Robinson, M. S., Denevi, B. W., & Team, L. S. (2011). LUNAR Reconnaissance Orbiter Camera global morphological map of the Moon. In *42nd Lunar and Planetary Science Conference, held March 7–11 at The Woodlands, Texas*. LPI Contribution (Vol. No. 1608, p. 2387).
- Sunshine, J. M., Pieters, C. M., & Pratt, S. F. (1990). Deconvolution of mineral absorption bands: An improved approach. *Journal of Geophysical Research*, 95(B5), 6955–6966. <https://doi.org/10.1029/JB095iB05p06955>
- Taguchi, M., Morota, T., & Kato, S. (2017). Lateral heterogeneity of lunar volcanic activity according to volumes of mare basalts in the farside basins. *Journal of Geophysical Research: Planets*, 122(7), 1505–1521. <https://doi.org/10.1002/2016JE005246>
- Terada, K., Anand, M., Sokol, A. K., Bischoff, A., & Sano, Y. (2007). Cryptomare magmatism 4.35 Gyr ago recorded in lunar meteorite Kalahari 009. *Nature*, 450(7171), 849–852. <https://doi.org/10.1038/nature06356>
- Tian, H. C., Wang, H., Chen, Y., Yang, W., Zhou, Q., Zhang, C., et al. (2021). Non-KREEP origin for Chang'e-5 basalts in the Procellarum KREEP Terrane. *Nature*, 600(7887), 59–63. <https://doi.org/10.1038/s41586-021-04119-5>



- U, K., Hasumi, H., & Ogawa, M. (2022). Effects of magma-generation and migration on the expansion and contraction history of the Moon. *Earth, Planets and Space*, 74(1), 78. <https://doi.org/10.1186/s40623-022-01631-4>
- Wang, Y., Wu, B., Xue, H., Li, X., & Ma, J. (2021). An improved global catalog of lunar impact craters ( $\geq 1$  km) with 3D morphometric information and updates on global crater analysis. *Journal of Geophysical Research: Planets*, 126(9), 1–25. <https://doi.org/10.1029/2020JE006728>
- Watanabe, T., Masuyama, T., Nagaoka, K., & Tahara, T. (2002). Analog experiments on magma-filled cracks: Competition between external stresses and internal pressure. *Earth, Planets and Space*, 54(12), 1247–1261. <https://doi.org/10.1186/bf03352453>
- Whitten, J., & Head, J. W. (2015a). Lunar cryptomaria: Mineralogy and composition of ancient volcanic deposits. *Planetary and Space Science*, 106, 67–81. <https://doi.org/10.1016/j.pss.2014.11.027>
- Whitten, J., & Head, J. (2015b). Lunar cryptomaria: Physical characteristics, distribution, and implications for ancient volcanism. *Icarus*, 247, 150–171. <https://doi.org/10.1016/j.icarus.2014.09.031>
- Wilhelms, D. E. (1987). *The geological history of the Moon*. United States Government Printing Office.
- Wilhelms, D. E., & Byrne, C. J. (2009). Stratigraphy of lunar craters. Retrieved from <http://www.imageagain.com/Strata/StratigraphyCraters.2.0.htm>
- Wilhelms, D. E., & El-Baz, F. (1977). *Geologic map of the east side of the Moon*. IMAP. <https://doi.org/10.3133/i948>
- Wilson, L., & Head, J. W. (2017). Generation, ascent and eruption of magma on the Moon: New insights into source depths, magma supply, intrusions and effusive/explosive eruptions (Part I: Theory). *Icarus*, 283, 146–175. <https://doi.org/10.1016/j.icarus.2015.12.039>
- Wünnemann, K., Collins, G. S., & Melosh, H. J. (2006). A strain-based porosity model for use in hydrocode simulations of impacts and implications for transient crater growth in porous targets. *Icarus*, 180(2), 514–527. <https://doi.org/10.1016/j.icarus.2005.10.013>
- Wünnemann, K., Zhu, M. H., & Stöffler, D. (2016). Impacts into quartz sand: Crater formation, shock metamorphism, and ejecta distribution in laboratory experiments and numerical models. *Meteoritics and Planetary Science*, 51(10), 1762–1794. <https://doi.org/10.1111/maps.12710>
- Xu, M., Jing, Z., Van Orman, J. A., Yu, T., & Wang, Y. (2022). Experimental evidence supporting an overturned iron-titanium-rich melt layer in the deep lunar interior. *Geophysical Research Letters*, 49(13), 1–10. <https://doi.org/10.1029/2022GL099066>
- Yamamoto, S., Nakamura, R., Matsunaga, T., Ogawa, Y., Ishihara, Y., Morota, T., et al. (2015). Global occurrence trend of high-Ca pyroxene on lunar highlands and its implications. *Journal of Geophysical Research: Planets*, 120(5), 831–848. <https://doi.org/10.1002/2014JE004740>
- Yamamoto, S., & Watanabe, S. (2021). Characterization of D-type spectra based on hyperspectral remote sensing of the lunar surface. *Journal of Geophysical Research: Planets*, 126(1), e2020JE006669. <https://doi.org/10.1029/2020JE006669>
- Yamamoto, S., Watanabe, S., & Matsunaga, T. (2018). Space-weathered anorthosite as spectral D-type material on the Martian satellites. *Geophysical Research Letters*, 45(3), 1305–1312. <https://doi.org/10.1002/2017GL076612>
- Yokota, Y., Matsunaga, T., Ohtake, M., Haruyama, J., Nakamura, R., Yamamoto, S., et al. (2011). Lunar photometric properties at wavelengths 0.5–1.6  $\mu\text{m}$  acquired by SELENE Spectral Profiler and their dependency on local albedo and latitudinal zones. *Icarus*, 215(2), 639–660. <https://doi.org/10.1016/j.icarus.2011.07.028>
- Zhang, B., Lin, Y., Moser, D. E., Warren, P. H., Hao, J., Barker, I. R., et al. (2021). Timing of lunar Mg-suite magmatism constrained by SIMS U–Pb dating of Apollo norite 78238. *Earth and Planetary Science Letters*, 569, 117046. <https://doi.org/10.1016/j.epsl.2021.117046>
- Zhang, D., Su, B., Chen, Y., Yang, W., Mao, Q., & Jia, L. H. (2022). Titanium in olivine reveals low-Ti origin of the Chang’E-5 lunar basalts. *Lithos*, 414–415, 106639. <https://doi.org/10.1016/j.lithos.2022.106639>
- Zhang, N., Ding, M., Zhu, M. H., Li, H., Li, H., & Yue, Z. (2022). Lunar compositional asymmetry explained by mantle overturn following the South Pole–Aitken impact. *Nature Geoscience*, 15(1), 37–41. <https://doi.org/10.1038/s41561-021-00872-4>
- Zhang, N., Parmentier, E. M., & Liang, Y. (2013a). A 3-D numerical study of the thermal evolution of the Moon after cumulate mantle overturn: The importance of rheology and core solidification. *Journal of Geophysical Research: Planets*, 118(9), 1789–1804. <https://doi.org/10.1002/jgre.20121>
- Zhang, N., Parmentier, E. M., & Liang, Y. (2013b). Effects of lunar cumulate mantle overturn and megaregolith on the expansion and contraction history of the Moon. *Geophysical Research Letters*, 40(19), 5019–5023. <https://doi.org/10.1002/grl.50988>
- Zhao, Y., de Vries, J., van den Berg, A. P., Jacobs, M. H. G., & van Westrenen, W. (2019). The participation of ilmenite-bearing cumulates in lunar mantle overturn. *Earth and Planetary Science Letters*, 511, 1–11. <https://doi.org/10.1016/j.epsl.2019.01.022>
- Zhu, M. H., Wünnemann, K., & Potter, R. W. K. (2015). Numerical modeling of the ejecta distribution and formation of the Orientale basin on the Moon. *Journal of Geophysical Research: Planets*, 120(12), 2118–2134. <https://doi.org/10.1002/2015JE004827>
- Zuber, M. T., Smith, D. E., Watkins, M. M., Asmar, S. W., Konopliv, A. S., Lemoine, F. G., et al. (2013). Gravity field of the moon from the Gravity Recovery and Interior Laboratory (GRAIL) mission. *Science*, 339(6120), 668–671. <https://doi.org/10.1126/science.1231507>

## References From the Supporting Information

- Jackson, A. P., Perera, V., & Gabriel, T. S. J. (2023). Impact generation of holes in the early lunar crust: Scaling relations. *Journal of Geophysical Research: Planets*, 128(4), 1–20. <https://doi.org/10.1029/2022JE007498>
- Kring, D. A., Kramer, G. Y., Collins, G. S., Potter, R. W. K., & Chandnani, M. (2016). Peak-ring structure and kinematics from a multi-disciplinary study of the Schrödinger impact basin. *Nature Communications*, 7(1), 13161. <https://doi.org/10.1038/ncomms13161>
- Oran, R., Weiss, B. P., Shprits, Y., Miljković, K., & Tóth, G. (2020). Was the moon magnetized by impact plasmas? *Science Advances*, 6(40), 1–11. <https://doi.org/10.1126/sciadv.abb1475>